Cell Reports
Physical Science

CellPress

Article

Inhibiting Freeze-Thaw Damage in Cement Paste and Concrete by Mimicking Nature's Antifreeze

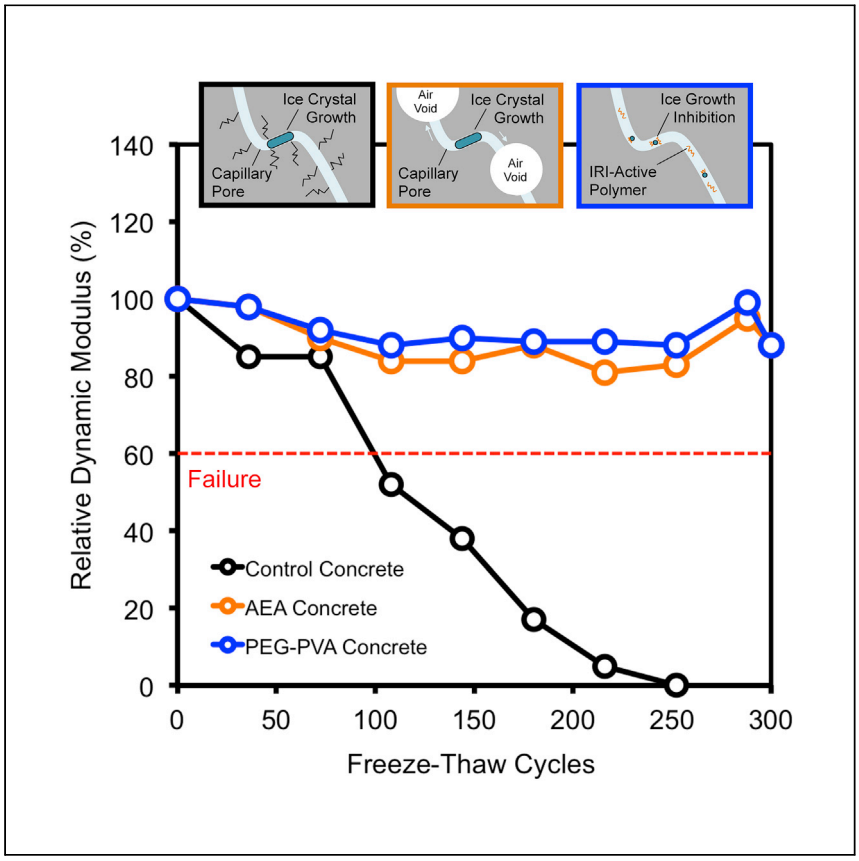

For nearly a century, microscopic air bubbles have been used to prevent cyclic freeze-thaw damage in cement paste and concrete. Frazier et al. demonstrate that a soluble, biomimetic ice-binding polymer that displays ice recrystallization inhibition and dynamic ice shaping imparts freeze-thaw resistance in cement paste and concrete without entraining air.

Shane D. Frazier, Mohammad G. Matar, Jorge Osio-Norgaard, Anastasia N. Aday, Elizabeth A. Delesky, Wil V. Srubar III

wsrubar@colorado.edu

HIGHLIGHTS

Antifreeze proteins inhibit ice growth via ice recrystallization inhibition (IRI)

Proteins lose functionality at a pH characteristic of cement paste (pH ~12.5)

PEG-PVA in solution displays biomimetic IRI and dynamic ice shaping at pH ~12.5

PEG-PVA molecules inhibit freeze-thaw damage in cement paste and concrete

Frazier et al., Cell Reports Physical Science 1, 100060
June 24, 2020
https://doi.org/10.1016/j.xcrp.2020.100060

Please cite this article in press as: Frazier et al., Inhibiting Freeze-Thaw Damage in Cement Paste and Concrete by Mimicking Nature's Antifreeze, Cell Reports Physical Science (2020), https://doi.org/10.1016/j.xcrp.2020.100060

Cell Reports
Physical Science

Article

Inhibiting Freeze-Thaw Damage in Cement Paste and Concrete by Mimicking Nature's Antifreeze

Shane D. Frazier,[1] Mohammad G. Matar,[2] Jorge Osio-Norgaard,[2] Anastasia N. Aday,[1] Elizabeth A. Delesky,[1] and Wil V. Srubar III[1,2,3,*]

SUMMARY

Since the 1930s, surfactant-based air-entraining admixtures (AEAs) have been used to mitigate freeze-thaw damage in cementitious materials. While effective, entrained air voids weaken concrete and increase its permeability, thereby increasing susceptibility to multiple other forms of *in situ* degradation. Inspired by nature, we report that a soluble biomimetic antifreeze polymer that displays ice recrystallization inhibition (IRI) and dynamic ice shaping (DIS) activities can prevent damage from ice crystal growth in cement paste and concrete. We first report that polyethylene glycol-graft-polyvinyl alcohol (PEG-PVA) mimics the explicit IRI and DIS activity of native ice-binding proteins in high-pH media characteristic of concrete pore solution. Second, we report that addition of PEG-PVA to cement paste and concrete prevents freeze-thaw damage without entraining air. Taken together, the findings demonstrate an alternative mechanistic approach to AEAs that can be leveraged to prevent damage from ice crystal growth in cementitious materials.

INTRODUCTION

Concrete—a mixture of water, aggregates, and ordinary portland cement (OPC)—is one of the most consumed materials on Earth,[1] and the economic and environmental consequences of its ubiquity are significant. The production of OPC alone accounts for 4%–8.6% of global CO_2 emissions, and its use places a burdensome toll on potable water resources, especially in water-scarce communities.[2–5] As the global population continues to rise, cement production is estimated to increase ~50% by 2050 to keep pace with new and aging infrastructure needs in both developing and developed countries.[1] In all parts of the world, the long-term resilience of cementitious materials remains critical to minimizing economic and environmental costs associated with unplanned damage and maintenance, especially in light of a changing climate that may exacerbate exposure conditions and lead to premature deterioration.

Cementitious materials exposed to cyclic freezing and thawing are highly susceptible to damage. It is well known that the formation and growth of ice crystals within the pores of cementitious materials can create hydraulic, osmotic, and crystallization pressures high enough to induce microscale cracks.[6,7] Cracking accelerates deterioration by reducing bulk mechanical integrity, exacerbating water and ion penetration, and increasing susceptibility to damage upon exposure to subsequent freeze-thaw cycles.

[1]Materials Science and Engineering Program, University of Colorado Boulder, UCB 027, Boulder, CO 80303, USA

[2]Department of Civil, Environmental, and Architectural Engineering, University of Colorado Boulder, UCB 428, Boulder, CO 80309, USA

[3]Lead Contact

*Correspondence: wsrubar@colorado.edu

https://doi.org/10.1016/j.xcrp.2020.100060

The prevailing strategy to enhance the freeze-thaw resistance of OPC concrete is to entrain an air void system in the paste that effectively reduces the pressures that develop during cyclic freezing and thawing of water in capillary pores. Conventional air-entraining admixtures (AEAs) create stabilized air void systems within cementitious matrices via surfactant mechanisms. AEAs must produce air voids of specific size distributions with proper spacing.[8–10] AEAs entrain ~16%–25% by volume of cement paste or ~4%–10% by volume of concrete.[10,11] Despite enhancing freeze-thaw resistance, the introduction of an air void system results in reduced mechanical strength, which can be as high as 5% per 1% entrained air and an increase in permeability that is proportional to the amount of introduced air.[12]

Researchers have utilized a variety of other materials and methods—often in tandem with AEAs—to enhance the freeze-thaw resistance of cementitious materials. These strategies include (1) densifying and strengthening cement paste using nanoparticles or supplementary cementitious materials,[13–16] (2) incorporating superabsorbent hydrogel particles as a non-surfactant method to achieve an entrained air void system,[17] and (3) using macroscale polymeric fibers for mitigating crack propagation due to frost-induced damage.[18,19] Despite some success, all of these methods aim at mitigating deleterious *symptoms* of ice expansion in cement paste and concrete rather than inhibiting the *source*—ice crystal growth.

Antifreeze proteins (AFPs) and antifreeze glycoproteins (AFGPs) are a subset of ice-binding proteins (IBPs) produced by plants, fish, insects, and bacteria that enable a variety of organisms to survive freezing temperatures.[20] By binding to the surface of ice, AFPs and AFGPs can inhibit the growth and coalescence of ice crystals (i.e., Ostwald ripening) via a process called ice recrystallization inhibition (IRI). AFPs and AFGPs also induce dynamic ice shaping (DIS) and reduce the freezing point of ice below the equilibrium freezing point (i.e., thermal hysteresis).[21] While recent work suggests that ice-binding and antifreeze properties are a result of anchored clathrate and ice-like motifs in AFPs,[22,23] specific mechanisms by which AFPs inhibit ice recrystallization have yet to be fully explicated.[24]

Researchers have successfully isolated AFPs and AFGPs from a multitude of freeze-tolerant organisms, which renders their incorporation into cementitious materials feasible. However, proteins are well known to restructure in non-native environments,[25] yielding high alkalinity (pH >12.5) of concrete pore solution unfavorable for protein stability.[26] Other studies have shown that some proteinaceous materials behave like set-retarding admixtures in fresh concrete, further limiting their applicability.[27]

To overcome economic limitations and instabilities of proteins in non-native environments, researchers have synthesized polymers that mimic the IRI and DIS activity of AFPs and AFGPs.[28,29] The most widely studied polymer displaying IRI and DIS activity is polyvinyl alcohol (PVA). The pendant hydroxyl groups along the polymer backbone of PVA mimic the highly hydroxylated carbohydrates of AFGPs.[28]

Although PVA displays IRI and DIS activity, two potential disadvantages exist when considering its use in cementitious systems, namely, (1) although PVA is soluble in water, mild heating is needed for it to solubilize, and (2) PVA is known to readily form cryogels when exposed to cyclic freezing and thawing temperatures.[30,31] To this end, we hypothesized that a polyethylene glycol-PVA graft copolymer (PEG-PVA), a commercially available water-soluble polymer commonly used as a pharmaceutical excipient,[32] would combine the IRI activity of PVA with the higher solubility

Please cite this article in press as: Frazier et al., Inhibiting Freeze-Thaw Damage in Cement Paste and Concrete by Mimicking Nature's Antifreeze, Cell Reports Physical Science (2020), https://doi.org/10.1016/j.xcrp.2020.100060

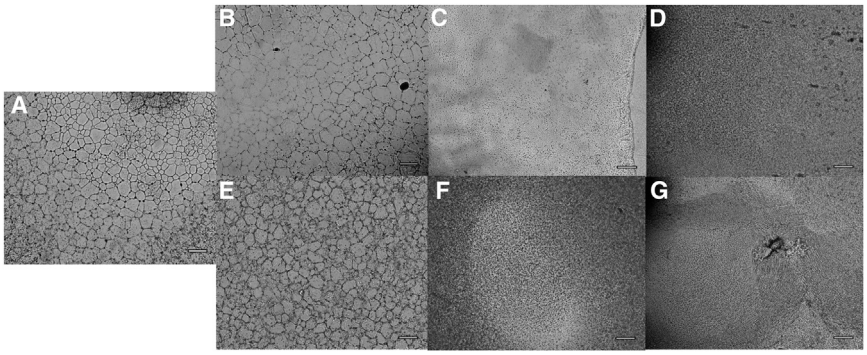

Figure 1. Optical Micrographs of IRI Splat Assay of PEG, PVA, and PEG-PVA in PBS

(A–G) Images show individual ice crystal grains that form in (A) PBS control solution, (B) 0.25 mg/mL PEG (PEG-L), (C) 0.25 mg/mL PVA (PVA-L), (D) 0.25 mg/mL PEG-PVA (PEG-PVA-L), (E) 0.50 mg/mL PEG (PEG-H), (F) 0.50 mg/mL PVA (PVA-H), and (G) 0.50 mg/mL PEG-PVA (PEG-PVA-H) in PBS after 30 min of annealing at −4°C. Scale bars, 100 μm.

of PEG so that it would inhibit frost-induced damage when used as a polymeric additive to cement paste and concrete.

In this work, we first illustrate the reduction in IRI activity of two native AFPs, *Shewanella frigidimarina* (SfIBP) and *Marinomonas primoryensis* (MpIBP), in high-pH solutions. Contrastingly, we show that PEG-PVA exhibits both IRI and DIS in neutral and high-pH solutions and, when used as a polymeric additive to cement paste and concrete, inhibits cyclic freeze-thaw damage while entraining <1% air in paste and <3% air in concrete by volume.

RESULTS

IRI of Proteins and Polymers

Splat-assay micrographs showing the IRI activity of polymers PEG, PVA, and PEG-PVA at neutral pH are shown in Figure 1. For reference, splat-assay micrographs of the proteins SfIBP and MpIBP in neutral pH solution are shown in Figure S1. The chemical structures of PEG, PVA, and PEG-PVA are shown in Figure S2. As expected, SfIBP,[26] MpIBP,[33] and PVA[28] exhibit IRI activity, while PEG[34] displays no IRI activity. PEG-PVA exhibited IRI activity (Figure 1) and reduced the average ice crystal grain size up to 90% when compared to a phosphate-buffered solution (PBS) control—an interesting result, given that the IRI activity of PEG-PVA has not yet been reported.

The IRI activities of all proteins and polymers were also screened in pH 13 solutions to determine whether their IRI activities would be affected by the highly alkaline environment characteristic of OPC pore solution. As expected, SfIBP and MpIBP lost IR activity (see Figure S3). The IRI activities of both PVA and PEG-PVA, however, were unaffected by the pH 13 solution (see Figure 2). The results for PVA were anticipated, as Burkey et al. previously demonstrated that the IRI activity of PVA increases in pH 13 solutions when compared to pH 7 and pH 1 solutions.[35] While PEG did not display IRI activity, data substantiate that a PEG-PVA copolymer retains the IRI activity of PVA in a highly alkaline solution. More specifically, PEG-PVA shows an 88% reduction in the size of ice crystals compared to neat pH 13 solution.

DIS of Proteins and Polymers

As expected, both SfIBP and MpIBP displayed DIS in neutral buffer but lost their ability to interact with ice in an OPC pore solution simulant (i.e., saturated $Ca(OH)_2$) (see

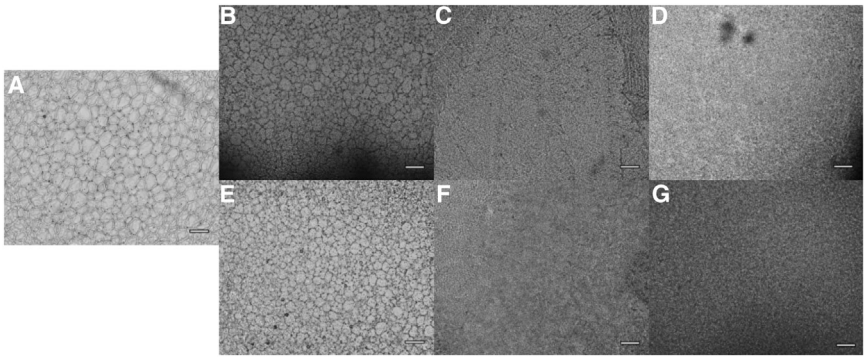

Figure 2. Optical Micrographs of IRI Splat Assay of PEG, PVA, and PEG-PVA in pH 13 Adjusted PBS Solution

(A–G) Images show individual ice crystal grains that form in (A) pH 13 control solution, (B) 0.25 mg/mL PEG (PEG-L), (C) 0.25 mg/mL PVA (PVA-L), (D) 0.25 mg/mL PEG-PVA (PEG-PVA-L), (E) 0.50 mg/mL PEG (PEG-H), (F) 0.50 mg/mL PVA (PVA-H), and (G) 0.50 mg/mL PEG-PVA (PEG-PVA-H) in pH 13 after 30 min of annealing at −4°C. Scale bars, 100 μm.

Figure S4). The combined loss of IRI and DIS activities in high pH and saturated $Ca(OH)_2$ rendered the native proteins unlikely to enhance freeze-thaw resistance in cement paste and concrete.

Figure 3 shows the DIS micrographs of each polymer in DI water at a concentration of 10 mg/mL and 10 mg/mL in saturated $Ca(OH)_2$ solution. Both PVA and PEG-PVA induced hexagonal shaping, indicating evidence of interaction of these molecules with ice crystal surfaces. Recent work has shown that the IRI activity of PVA is a result of hydroxyl group interaction with the prismatic faces of Ih (hexagonal) ice.[36,37] Together, the IRI and DIS results indicated good potential for PVA and PEG-PVA to enhance freeze-thaw resistance of cement paste and concrete via a new mechanism related to inhibition of ice crystal growth.

Freeze-Thaw Resistance of Cement Paste

First, we evaluated whether PEG, PVA, and/or PEG-PVA would mitigate freeze-thaw damage in cement paste. Figure 4 provides representative 2D cross-sectional micro X-ray computed tomography (MXCT) images of paste samples after exposure to 30 freeze-thaw cycles. Control paste and pastes containing both low (L) (0.01 wt.% cement) and high (H) (0.021 wt.% cement) additions of PEG and PVA exhibited signs of internal crack formation. Additionally, external spalling was observed in all of these samples, as can be seen in the inset images of Figure 4. OPC paste containing PEG-PVA at an addition of 0.021 wt.% of cement (PEG-PVA-H) exhibited no damage. All other samples exhibited signs of freeze-thaw damage, including crack formation within the scanned volumes and spalling of the surface (inset images of Figure 4).

Even though PVA was IRI active, it did not fully mitigate freeze-thaw damage in cement paste. Its inability to mitigate freeze-thaw damage in paste is possibly attributable to (1) insufficient molecular weight and (2) its propensity to form hydrogels, specifically when exposed to freeze-thaw cycling (i.e., cryogenic gelation).[30,31] Cryogenic gelation of PVA occurs due to the formation of crystalline structures upon repeated freeze-thaw cycles that subsequently behave as physical crosslinkers.[30] The internal formation and swelling of a hydrogel or cryogel within cement paste could induce cracking, as observed herein. Due to the addition of PEG, the ability of PEG-PVA to form a hydrogel or cryogel may have been reduced compared to PVA, given that PEG behaves as a plasticizing agent[32] to inhibit crystallization.

Please cite this article in press as: Frazier et al., Inhibiting Freeze-Thaw Damage in Cement Paste and Concrete by Mimicking Nature's Antifreeze, Cell Reports Physical Science (2020), https://doi.org/10.1016/j.xcrp.2020.100060

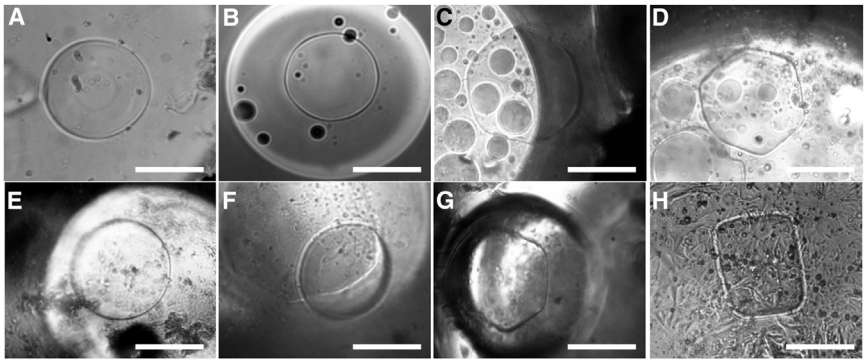

Figure 3. Optical Micrographs of DIS for Polymers

(A–D) Single ice crystals for (A) DI water, (B) 10 mg/mL PEG in DI, (C) 10 mg/mL PVA in DI, and (D) PEG-PVA at 10 mg/mL in DI. Both PVA and PEG-PVA display hexagonal ice shaping.

(E) Saturated $Ca(OH)_2$ solution.

(F) 10 mg/mL PEG in sat. $Ca(OH)_2$ solution.

(G) 10 mg/mL PVA in sat. $Ca(OH)_2$ solution.

(H) 10 mg/mL PEG-PVA in sat. $Ca(OH)_2$ solution.

Both PVA and PEG-PVA maintain their ability to shape ice in the presence of saturated $Ca(OH)_2$ solution. Note that in (C), (D), and (G) the c-axis of hexagonal ice crystal is aligned with the plane of image and in (H) it is perpendicular to the plane of image. Scale bars, 50 μm.

The percentage of volume of air, or air content, of paste samples was determined using MXCT by measuring the initial volume of pores with a diameter >50 μm. Figure 5 provides representative 3D reconstructions of the air void systems, colored pink, and the average air content for all samples. PEG, PVA, and PEG-PVA at both low (L) and high (H) concentrations introduce <0.8% air content in the paste. These observed air contents are lower than the industry accepted air contents of ~16%–25% air by volume of cement paste that are recommended for freeze-thaw resistance.[10] Additional air void data obtained by MXCT can be found in Table S6 and Figures S11–S17.

In addition to substantiating a negligible effect on initial compressive strength (Figure S9), we also confirmed no significant effect on the heat of hydration or time of set (Figure S6), flowability (Figures S7 and S8), and mineralogy (Table S5; Figure S10) of OPC paste with polymer additions.

Freeze-Thaw Resistance of Concrete

Next, we evaluated whether PEG-PVA would mitigate freeze-thaw damage in concrete. While it was determined that a minimum concentration of 0.021% PEG-PVA (by weight percentage of cement) was sufficient to inhibit freeze-thaw damage in paste, we evaluated the effect of increasing PEG-PVA concentration on the freeze-thaw resistance of concrete. PEG-PVA-modified samples were concurrently tested with unmodified (i.e., control) formulations and AEA-modified concrete. For reference, the initial compressive strength for all samples is shown in Figure S22.

In accordance with industry standards, the relative dynamic moduli of elasticity, durability factory, and length change were monitored during freeze-thaw cycling. The change in relative dynamic modulus of elasticity, P_c, a quantitative measure of mechanical integrity, during 300 freeze-thaw cycles is shown in Figure 6. P_c = 60% denotes the damage threshold, below which indicates failure due to freeze-thaw damage. One sample in each test group (P4) was kept at ambient conditions. As evidenced by data in Figure 6, the P_c of the control and 0.022% PEG-PVA samples

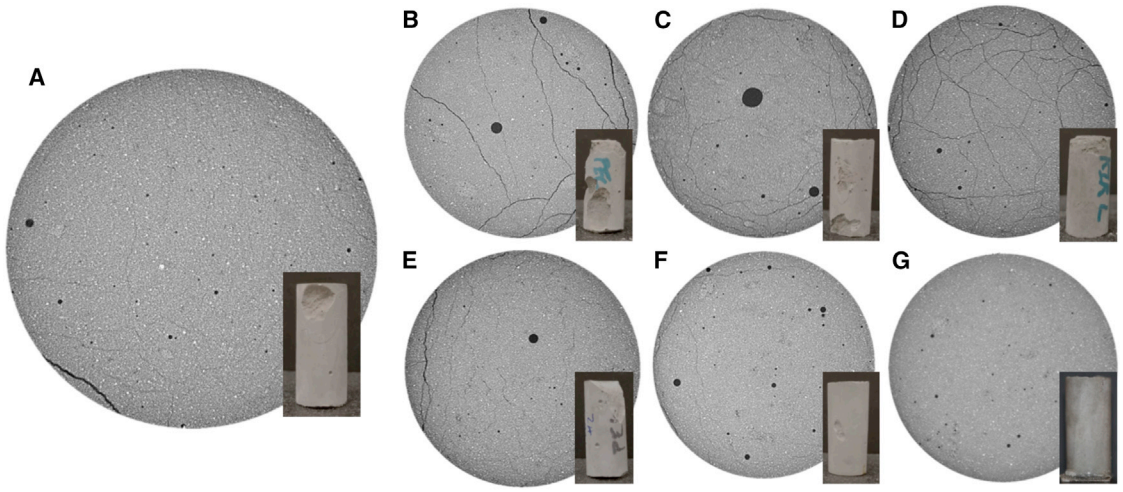

Figure 4. Post-Freeze-Thaw MXCT 2D Cross-Sectional Images

(A–G) Images of (A) control, (B) PEG-L, (C) PVA-L, (D) PEG-PVA-L, (E) PEG-H, (F) PVA-H, and (G) PEG-PVA-H cement paste formulations. Inset images show bulk samples post-freeze-thaw. MXCT cross-sections are 9 mm in diameter. Bulk samples are 16 mm in diameter by 32 mm in height.

dropped below 60% after 250 cycles of testing. However, the P_c of the all samples with PEG-PVA $\geq$0.066% and the AEA sample, as expected, remained above 60%, indicating acceptable resistance to freeze-thaw cycling.

Figure 7 shows the average durability factor for each test group. Similar to the results for P_c, samples containing 0.066%, 0.25%, and 1.0% PEG-PVA and AEA samples exhibited durability factors of 88.6%, 84.9%, and 89.2% and 86.2%, respectively, indicating freeze-thaw resistance. Both the control and 0.022% PEG-PVA sample yielded poor durability factors

Figure 7 shows the average length change of samples with increasing number of freeze-thaw cycles. Previous research has shown that an increase in length with increasing number of freeze-thaw cycles coincides with deterioration.[38,39] Samples containing PEG-PVA at additions of 0.066%–1.00% and AEA saw length changes <0.1%—the maximum threshold for freeze-thaw resistance. Both the control and 0.022% PEG-PVA samples exhibited length changes >0.1%, indicating unacceptable dimensional instability according to the standard.

According to data in Figures 6 and 7, samples containing 0.066%, 0.25%, and 1.00% PEG-PVA and the AEA sample all exhibited acceptable freeze-thaw performance, while the control formulation and the 0.022% PEG-PVA sample failed according to the standard.

The key question remained whether the PEG-PVA-containing samples that resisted freeze-thaw damage did so via air entrainment or a mechanism related to inhibiting ice crystal growth. To determine whether the PEG-PVA-modified concretes that met the specification did so by a mechanism other than entraining sufficient air, the fresh- and hardened-state air contents and void spacing factors for all samples were measured (see Table 1; see also Figure S21 and Table S8). To resist freeze-thaw damage via an AEA mechanism, a minimum fresh-state air content of 6.5% is recommended for air-entrained concrete with a nominal maximum aggregate size of <25 mm,[11] which was used in this study, and a maximum void spacing factor <250 μm is recommended.[40,41] In general, a hardened-state air content of ~4%–10% ensures adequate resistance to freeze-thaw damage.[11,42]

Please cite this article in press as: Frazier et al., Inhibiting Freeze-Thaw Damage in Cement Paste and Concrete by Mimicking Nature's Antifreeze, Cell Reports Physical Science (2020), https://doi.org/10.1016/j.xcrp.2020.100060

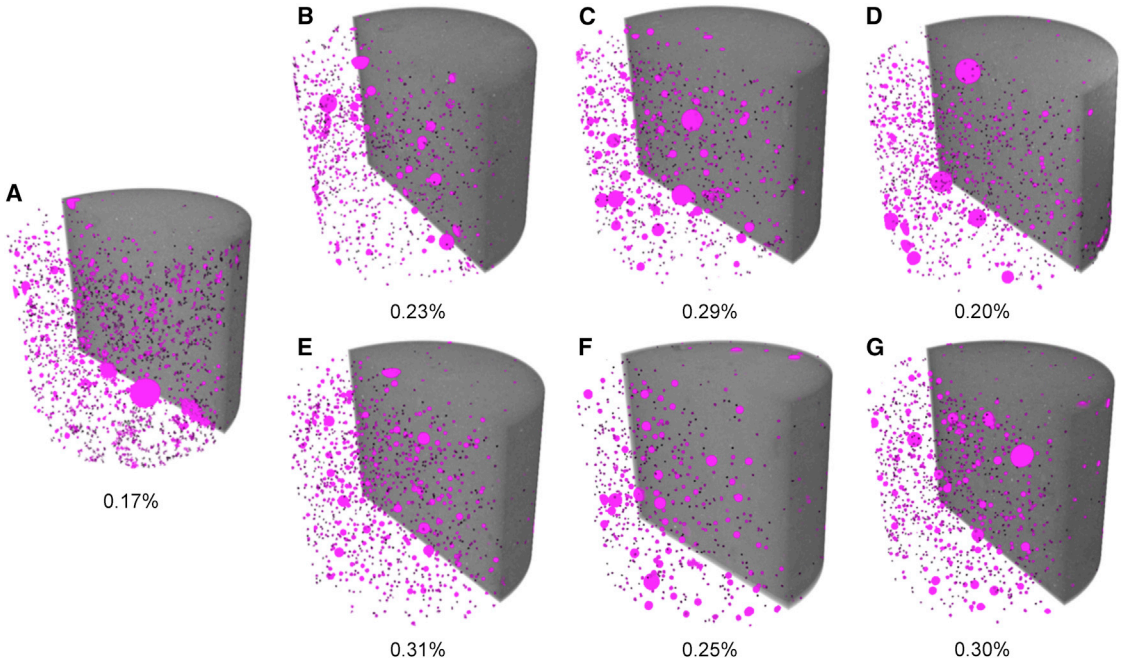

Figure 5. MXCT 3D Reconstructions of Air Void Systems and Calculated Air Content for Cement Paste Formulations

(A–G) Representative 3D reconstructions with air voids highlighted in pink for (A) control, (B) PEG-L, (C) PVA-L, (D) PEG-PVA-L, (E) PEG-H, (F) PVA-H, and (G) PEG-PVA-H. Each cylindrical scanned volume is 9 mm in diameter and 8 mm in height. The average (n = 2) percentage volume of air, or air content, is shown under each reconstruction.

The AEA sample contained 7.0% and 4.0% air in the fresh- and hardened-state, respectively, and exhibited a spacing factor of 218 μm, thereby meeting the industry recommendation, as anticipated. In contrast, the 0.066% PEG-PVA sample exhibited fresh- and hardened-state air contents of 4.2% and 3.2%, respectively, as well as a 392 μm spacing factor (>250 μm), substantiating that the 0.066% PEG-PVA sample prevented freeze-thaw damage in concrete samples without a properly entrained air void system.

DISCUSSION

Together with the IRI and DIS data, the freeze-thaw resistance testing and air void content analysis reveals that, in sufficient dosages, PEG-PVA can resist freeze-thaw damage in OPC paste and concrete by a mechanism that is distinct from AEAs. While AEAs stabilize an air void system that helps dissipate hydraulic and osmotic pressures that are generated by ice crystal growth and coalescence, the results presented herein substantiate that PEG-PVA-modified concrete impart freeze-thaw resistance to concrete via IRI and DIS activity. Given that PEG-PVA exhibited IRI and DIS activity in high-pH solutions characteristic of OPC pore solution, the resistance of PEG-PVA-modified concrete to resist freeze-thaw damage is mechanistically attributable to the ability of PEG-PVA to inhibit ice crystal growth.

These results suggest that biomimetic antifreeze molecules, like PEG-PVA, can inhibit freeze-thaw damage in cement paste and concrete. Use of these molecules may help counter other deleterious disadvantages that coincide with the use of AEAs. For example, despite achieving target air void contents, some AEAs do not necessarily mitigate freeze-thaw damage—a result that suggests the chemical properties of AEAs may play a critical role in their effectiveness.[10] In addition, it is well known that reductions in compressive strength, increased permeability, and

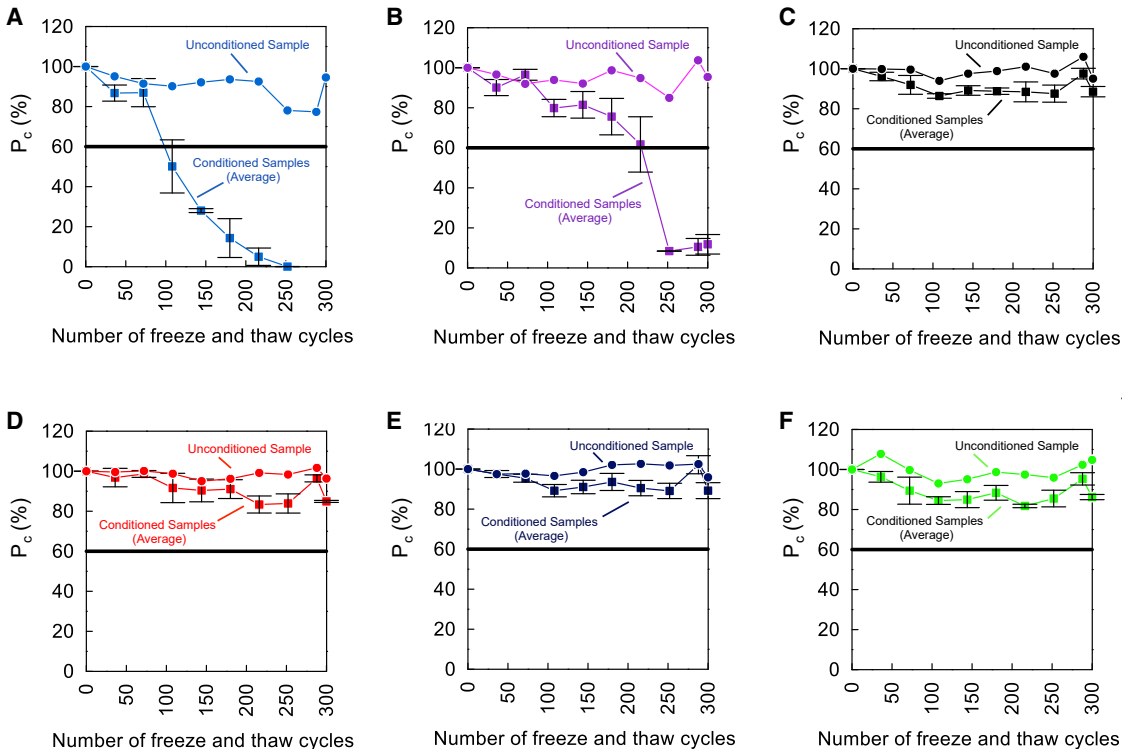

Figure 6. Average Relative Dynamic Modulus of Elasticity for Each Concrete Test Group

(A) Control.

(B) 0.022% PEG-PVA.

(C) 0.066% PEG-PVA.

(D) 0.25% PEG-PVA.

(E) 1.0% PEG-PVA.

(F) AEA.

Three samples within each test group were subjected to freeze-thaw cycling. One sample in each test group was left at ambient conditions. The horizontal lines at 60% P_c represent failure criteria. Error bars represent the standard deviation of n = 3 replicates.

retardation of setting time can occur with the use of AEAs[12,43]—behaviors that were not exhibited herein by the use of PEG-PVA in cement paste. Furthermore, recent research has indicated that, if a critical water saturation level is reached in air-entrained concrete (~86%–88%), entrained air void systems are rendered ineffective and freeze-thaw damage is inevitable.[44,45] While the time to reach this critical water saturation level can be years,[44,46] the propensity for unavoidable damage in saturated air-entrained concrete is a limitation to the use of AEAs.

In summary, the results from this work indicate that robust IRI- and DIS-active molecules with an ability to interact directly with ice and prevent its continued growth and coalescence can provide an alternative mechanistic approach to freeze-thaw mitigation in cement paste and concrete—a finding that motivates further research and development into biomimetic antifreeze admixture technologies that may supplant the decades-long use of AEAs.

EXPERIMENTAL PROCEDURES

Resource Availability

Lead Contact

Further information and requests for resources and reagents should be directed to and will be fulfilled by the Lead Contact, Prof. Wil Srubar (wsrubar@colorado.edu).

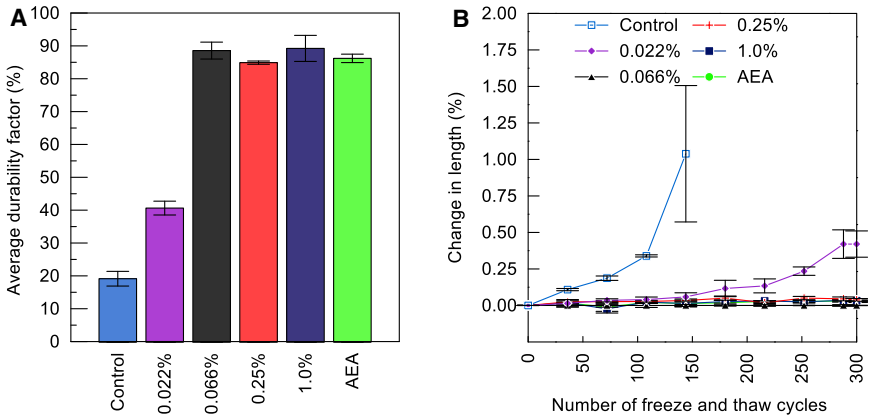

Figure 7. Durability Factor and Length Change

(A and B) Average durability factor (%) (A) for each concrete group and average length change (%) (B) for each concrete group. Error bars represent the standard deviation of n = 3 replicates.

Materials Availability

This study did not generate new unique reagents.

Data and Code Availability

The authors declare that data supporting the findings of this study are available within the paper and the Supplemental Information. All other data are available from the lead contact upon reasonable request.

Materials

PEG-PVA (CAS # 96734-39-3), PEG (CAS # 25322-68-3), and PVA (CAS # 9002-89-5) were purchased from Sigma-Aldrich and used without any modification. MasterAir AE 200 was obtained from BASF. Research grade $Ca(OH)_2$ was purchased from Fisher Scientific. The cement used in this study was a commercially available Type I/II OPC (Quikrete) that complies with ASTM C150.[47] The chemical composition of the OPC is reported in Table S3. Both fine and coarse aggregates were acquired from Martin Marietta (Golden, CO, USA). Coarse aggregate had a nominal maximum size <25 mm. Additional aggregate details can be found in Table S4.

Antifreeze Proteins

SfIBP at a concentration of 4 mg/mL in solution was obtained from Dr. Peter Davies at Queen's University in Kingston, Ontario, Canada[33] and was reconstituted using a centrifugal filter into 20 mM tris(hydroxymethyl)aminomethane (Tris) solution. SfIBP concentration was verified at 4.4 mg/mL against a protein standard, bovine serum albumin, using UV-Vis.

Clonal cells were obtained from Dr. Peter Davies at Queen's University in Kingston, Ontario, Canada and used to express the ice-binding region (region IV) from *Marinomonas primoryensis* (MpIBP).[48] Expression and purification of MpIBP were adapted from Garnham et al.[48] Protein expression and purification methods can be found in the Supplemental Experimental Procedures, Table S1, and Figure S5).

IRI

A modified ice recrystallization assay was performed to observe IRI activity of proteins and polymers.[49] All samples were analyzed in triplicate. 10 μL of sample was dropped from 1.7 m onto a glass slide (thickness of 1 mm). The glass slide was pre-cooled on an aluminum block at −78°C. The slide was then immediately

Table 1. Fresh- and Hardened-State Air Content of Concrete

Test Group	Fresh State Air Content (%)	Hardened State Air Content (%)	Spacing Factor (μm)
Control	2.1	2.7	1,061
0.022% PEG-PVA	3.0	1.5	400
0.066% PEG-PVA	4.2	2.3	392
0.25% PEG-PVA	13	5.2	308
1.0% PEG-PVA	30	19.6	191
AEA	7.0	4.0	218

transferred to an Otago nanoliter osmometer cold stage and annealed at −4°C (air temperature) for 30 min. Images were collected immediately after the sample was placed on the cold stage (t_0) and again at 30 min (t_{30}) to observe ice recrystallization. For all samples except those containing SfIBP, images were obtained using an Olympus BX41 microscope with ELWD U Plan 20×/0.45 objective and crossed polarizers, equipped with an OMAX A35140U camera on a 0.5× C-mount adaptor. SfIBP sample images were obtained using a Zeiss Axio Imager M2m microscope with an EC Epiplan 5×/0.13 BD M27 objective and crossed polarizers, equipped with an Axiocam 506 color camera on a 1 in 1.0× 60N C-mount adaptor. ImageJ 1.48v software (National Institutes of Health) was used to place scale bars and estimate the grain sizes.

The proteins and polymers were tested in a neutral buffer and a pH 13 adjusted buffer solution. A description of each protein solution (neutral and pH 13) can be found in Table S2. Polymers were tested in PBS and the pH 13 solution was made with addition of NaOH. Studying the ability of materials to inhibit ice recrystallization in saturated $Ca(OH)_2$ to simulate the chemistry of synthetic OPC pore solution[50] proved difficult due to the precipitation of crystalline solids at subzero temperatures.

For SfIBP, a concentration of 0.125 mg/mL was selected in this study to evaluate ice crystal nucleation and growth inhibition, as it ensured protein activity would be at a maximum[33] for evaluating changes in protein performance in extreme environments. Similarly, a concentration of 0.10 mg/mL was chosen for MpIBP.[48] Concentrations of 0.25 and 0.50 mg/mL were chosen for PEG, PVA, and PEG-PVA based on concentrations previously studied for PEG and PVA[28].

DIS

DIS occurs when a material interacts with one or more crystallographic planes of ice resulting in a change to the morphology of a single ice crystal. To observe DIS, a nanoliter-sized drop of sample was placed in microscopy immersion oil (Sigma) where both are in a hole of ~0.5 mm diameter within an aluminum disk. The aluminum disk was placed on an Otago nanoliter osmometer cold stage, where the temperature of the cold stage was rapidly cooled to −20°C to form polycrystalline ice. Next, the sample was slowly melted to form a single ice crystal by heating at a rate of approximately 5°C/min. Once a single ice crystal was obtained the temperature was kept constant for 3 min to ensure stability. Last, the sample was cooled at 0.01°C/min until crystal growth and/or ice shaping was observed. Proteins were tested in buffer solutions and a buffer solution with saturated $Ca(OH)_2$. The constituents of the protein buffer solutions can be found in Table S2. Concentrations of 0.125 and 0.10 mg/mL were tested for SfIBP and MpIBP, respectively. The polymers were tested in DI water and a saturated $Ca(OH)_2$ solution. A concentration of 10 mg/mL was tested for all polymers due to previous studies of the DIS abilities of PVA.[51]

Table 2. Cement Paste Mix Design Formulations

Sample	w/c Ratio	Polymer (wt.% of cement)
Control	0.42	–
PEG-L	0.42	0.010%
PEG-H	0.42	0.021%
PVA-L	0.42	0.010%
PVA-H	0.42	0.021%
PEG-PVA-L	0.42	0.010%
PEG-PVA-H	0.42	0.021%

Cement Paste and Concrete Sample Preparation

All OPC paste samples were hand mixed for 3 min with a 0.42 water to cement ratio (w/c) and cured for 14 days in a 99% relative humidity chamber prepared according to ASTM C192 at 20°C ± 2°C.[52] Freeze-thaw resistance, air content, and compressive strength samples were cast in cylindrical polyethylene molds 32 mm in height and 16 mm in diameter complying with the ratios of height to diameter provided in ASTM C39.[53] Table 2 provides the sample compositions of cement paste samples. The amounts of PEG, PVA, and PEG-PVA chosen in the mix design were based on the concentrations used for IRI testing (i.e., 0.25 mg/mL = 0.010 wt.% polymer in mixing water).

Concrete specimens were prepared using the mix compositions described in Table 3. All components were weighed using a balance (Adam Equipment CBC 35a) and mixed using a commercially available mixer (YardMax YM0115). PEG-PVA was added to the mixing water and stirred until dissolved. Coarse aggregate was pre-wetted with a small amount of mixing water prior to mixing. After the initiation of mixing, fine aggregate and cement were placed in the mixer along with the rest of mixing water. Concrete ingredients were mixed for 3 min followed by a 3-min rest, where a trowel was used to hand-mix dry and wet components inside the mixer, followed by an additional 2 min of mixing. The same process was repeated until uniform consistency was achieved, in accordance with ASTM C192. Table S7 provides the measured slump values for each concrete test group. Slump tests were performed according to ASTM C143 using a slump test setup (Humboldt H-3645).

Concrete was placed into cylinder molds in three layers and prism molds in two layers. After the addition of each layer, the specimens were vibrated until proper consolidation was achieved. Specimens were stored at ambient conditions in a vibration-free environment and covered to prevent evaporation of water. After 48 h, specimens were removed from the molds and transferred to a saturated $Ca(OH)_2$ solution for the remainder of the curing process. Water was saturated with calcium hydroxide per ASTM C511 to prevent leaching of calcium hydroxide from specimens.[54] Cylindrical specimens were cured for 28 days per ASTM C 192[52] and prisms for 14 days per ASTM C666.[55] Each test group consisted of at least three 10.16 × 20.32 cm cylinders and four 7.62 × 7.62 × 40.64 cm specimens.

Freeze-thaw Resistance

Freeze-thaw cycling of OPC paste samples was performed in a custom-built chamber following a modified version of ASTM C666 procedure A.[55] Details of the chamber may be found in Figures S18 and S19. All samples were tested for a total of 30 cycles in which the freezing lasted for 1.5 h and thawing for 2.5 h, respectively. During freezing cycles, the temperature reached −15°C ± 2°C and thawing cycles 16.5°C ± 2°C, as measured with a DHT-22 temperature sensor (SparkFun

Table 3. Concrete Mix Design Formulations

Material	Control	0.022% PEG-PVA	0.066% PEG-PVA	0.25% PEG-PVA	1.0% PEG-PVA	AEA
Cement (type I/II) (kg/m^3)	309	309	309	309	309	309
Fine aggregate (kg/m^3) (moisture content 3.3%)	600	600	600	600	600	600
Coarse aggregate (kg/m^3) (moisture content 0.29%)	1,210	1,210	1,210	1,210	1,210	1,210
Water/cement ratio (%)	50	50	50	50	50	50
PEG-PVA/cement ratio (%)	0	0.022	0.066	0.25	1.00	0
AEA (mL/100 kg of cement)	0	0	0	0	0	15

Electronics, USA). To ensure samples remained saturated, a minimal water level was maintained in the bottom of the chamber.

Freeze-thaw cycling of concrete was performed following ASTM C666 Procedure A.[55] A modified Humboldt (HC-3186S.4F) freeze-thaw cabinet was used. Three prisms from each test group were subjected to 300 cycles, labeled P1–P3. An additional prism was kept at room temperature and labeled P4. The freezing portion of each cycle had a duration of 3 h and reached a minimum of $-18°C \pm 2°C$. The thawing portion of each cycle had a duration of 1 h and reached a maximum of $4°C \pm 2°C$. The temperature profile can be found in Figure S20. The water level prescribed in ASTM C666 Procedure A was maintained throughout testing.

Freeze-thaw resistance was evaluated by measuring the fundamental transverse frequency and length change of prism samples every 36 cycles, including measurements before freeze-thaw cycling. Fundamental transverse frequency was determined using the forced resonance method in accordance to ASTM C215[56] of prisms P1–P4 of each test group. The fundamental transverse frequency was used to calculate the relative dynamic modulus of elasticity (P_c) according to:

$$P_c = \left(\frac{n_1^2}{n^2}\right) \times 100, \qquad \text{(Equation 1)}$$

where n_1 is the fundamental transverse frequency at 0 cycles of freezing and thawing and n is the fundamental transverse frequency after c cycles of freezing and thawing.

The freeze-thaw cycling was continued until one of the following conditions was met: (1) samples undergo 300 freeze-thaw cycles or (2) relative dynamic modulus of elasticity falls below 60%. Length change was recorded in this study as an indicator of deterioration but was not necessarily used as criteria for ending the test. The durability factor, DF, was also calculated for each test group as outlined in ASTM C666[55] according to:

$$DF = \frac{PN}{M}, \qquad \text{(Equation 2)}$$

where P is relative dynamic modulus of elasticity at N cycles (%), N is the number of cycles at which P reaches the specified minimum value for discontinuing the test or the specified number of cycles at which the exposure is to be terminated, whichever is less, and M is the specified number of cycles at which the exposure is to be terminated.

Hardened-State Air Content

Micro X-ray computed tomography (MXCT) enabled 3D visualization of internal air void systems. The MXCT (ZEISS Xradia 520 Versa) source voltage was set to 140 kV and the power to 10 W. An objective with an optical magnification of 0.4× was used.

For paste samples, the source and detector locations were varied to obtain a desired resolution (voxel size) of approximately 4.6 μm. Samples were scanned using MXCT before and after freeze-thaw cycling. The scans performed before cycling were used to ensure cracking was not occurring due to other phenomenon (e.g., shrinkage). Internal cracks present in the samples post-freeze-thaw cycling indicated damage due to freeze-thaw cycling. For post-freeze-thaw concrete samples, the source and detector locations were varied to obtain a desired resolution (voxel size) of approximately 6 μm. Cubic samples cut from cylindrical specimen having volumes of approximately 17 cm^3.

The volume percentage of air in OPC paste and concrete samples, or air content, pre-freeze-thaw cycling was determined from the volume of all voids with diameters greater than 50 μm for paste and 15 μm for concrete. These diameters were chosen based on the accepted size range of air voids,[57] previous research,[58] and resolution capabilities of MXCT. Dragonfly 3.9 software (Object Research Systems) was used to generate the reconstructions, to calculate the scanned volume of sample (V_{sample}), and volume of all voids.

The MXCT 3D reconstructions were analyzed in Dragonfly 3.9 software to determine the air void distribution (i.e., frequency of voids for a given diameter range). MXCT 2D cross-sections were analyzed to determine the spacing factor and specific surface. The equations provided in the linear traverse method of ASTM C457 were used to calculate spacing factor without modification. This approach has previously been used to calculate the spacing factor.[59]

SUPPLEMENTAL INFORMATION

Supplemental Information can be found online at https://doi.org/10.1016/j.xcrp.2020.100060.

ACKNOWLEDGMENTS

This research was made possible by the Department of Civil, Environmental, and Architectural Engineering, the College of Engineering and Applied Sciences, and the Living Materials Laboratory at the University of Colorado Boulder with financial support from the National Science Foundation (award nos. CMMI-1727788 and CMMI-1726864) and the National Highway's Cooperative Research Program (NCHRP) (award no. NCHRP-204). Thanks to Tyler Vance, Rob Eves, and Peter Davies at Queen's University for the gifts of the *Shewanella frigidimarina* IBP and the *Marinomonas primoryensis* clones used in this study.

AUTHOR CONTRIBUTIONS

S.D.F., M.G.M., and W.V.S. III conceived and designed the experiments; S.D.F., M.G.M., J.O.-N., A.N.A., and E.A.D. performed the experiments; S.D.F., M.G.M., J.O., A.N.A., and E.A.D. analyzed the data; W.V.S. III contributed reagents, materials, and analysis tools; and S.D.F., M.G.M., J.O., A.N.A., E.A.D., and W.V.S. III wrote the paper.

CellPress
OPEN ACCESS

Cell Reports
Physical Science
Article

DECLARATION OF INTERESTS

The authors declare no competing interests.

Received: November 6, 2019
Revised: March 2, 2020
Accepted: April 8, 2020
Published: May 27, 2020

REFERENCES

1. Monteiro, P.J.M., Miller, S.A., and Horvath, A. (2017). Towards sustainable concrete. Nat. Mater. *16*, 698–699.

2. Davis, S.J., Lewis, N.S., Shaner, M., Aggarwal, S., Arent, D., Azevedo, I.L., Benson, S.M., Bradley, T., Brouwer, J., Chiang, Y.-M., et al. (2018). Net-zero emissions energy systems. Science *360*, eaas9793.

3. Andrew, R.M. (2018). Global CO_2 emissions from cement production. Earth Syst. Sci. Data *10*, 195.

4. Miller, S.A., Horvath, A., and Monteiro, P.J.M. (2016). Readily implementable techniques can cut annual CO_2 emissions from the production of concrete by over 20%. Environ. Res. Lett. *11*, 074029.

5. Miller, S.A., Horvath, A., and Monteiro, P.J.M. (2018). Impacts of booming concrete production on water resources worldwide. Nat. Sustain. *1*, 69–76.

6. Powers, T.C. (1975). Freezing Effects in concrete. In Durability of Concrete, *47*, pp. 1–12.

7. Scherer, G.W., and Valenza, J.J. (2005). Mechanism of frost damage. Mater. Sci. Concr. *7*, 209–246.

8. Powers, T.C. (1954). Void Spacing as a Basis for Producing Air-Entrained Concrete. J. Am. Concr. Inst. *25*, 741–760.

9. Du, L., and Folliard, K.J. (2005). Mechanisms of air entrainment in concrete. Cement Concr. Res. *35*, 1463–1471.

10. Chatterji, S. (2003). Freezing of air-entrained cement-based materials and specific actions of air-entraining agents. Cement Concr. Compos. *25*, 759–765.

11. ACI Committee 201 (2016). Guide to Durable Concrete (American Concrete Institute).

12. Wong, H.S., Pappas, A.M., Zimmerman, R.W., and Buenfeld, N.R. (2011). Effect of entrained air voids on the microstructure and mass transport properties of concrete. Cement Concr. Res. *41*, 1067–1077.

13. Sabir, B.B. (1997). Mechanical properties and frost resistance of silica fume concrete. Cement Concr. Res. *19*, 285–294.

14. Duan, P., Shui, Z., Chen, W., and Shen, C. (2013). Enhancing microstructure and durability of concrete from ground granulated blast furnace slag and metakaolin as cement replacement materials. J. Mater. Res. and Technol. *2*, 52–59.

15. Behfarnia, S. (2013). The effects of nano-silica and nano-alumina on frost resistance of normal concrete. Constr. Build. Mater. *48*, 580–584.

16. Gonzalez, M., Tighe, S., Hui, K., Rahman, S., and Lima, A.O. (2016). Evaluation of freeze/thaw and scaling response of nanoconcrete for Portland Cement Concrete (PCC) pavements. Constr. Build. Mater. *120*, 465–472.

17. Lausten, S., Hasholt, M.T., and Jensen, O.M. (2015). Void Structure of Concrete with Superabsorbent Polymers and Its Relation to Frost Resistance of Concrete. Mater. Struct. *48*, 357–368.

18. Nam, J., Kim, G., Lee, B., Hasegawa, R., and Hama, Y. (2016). Frost resistance of polyvinyl alcohol fiber and polypropylene fiber reinforced cementitious composites under freeze thaw cycling. Compos., Part B Eng. *90*, 241–250.

19. Wang, S., and Li, V.C. (1966). Polyvinyl alcohol fiber reinforced engineered cementitious composites: materials design and performance. Microchem. J. *11*, 264–268.

20. Davies, P.L. (2014). Ice-binding proteins: a remarkable diversity of structures for stopping and starting ice growth. Trends Biochem. Sci. *39*, 548–555.

21. Voets, I.K. (2017). From ice-binding proteins to bio-inspired antifreeze materials. Soft Matter *13*, 4808–4823.

22. Hudait, A., Odendahl, N., Qiu, Y., Paesani, F., and Molinero, V. (2018). Ice-Nucleating and Antifreeze Proteins Recognize Ice through a Diversity of Anchored Clathrate and Ice-like Motifs. J. Am. Chem. Soc. *140*, 4905–4912.

23. Hudait, A., Moberg, D.R., Qiu, Y., Odendahl, N., Paesani, F., and Molinero, V. (2018). Preordering of water is not needed for ice recognition by hyperactive antifreeze proteins. Proc. Natl. Acad. Sci. USA *115*, 8266–8271.

24. Marks, S.M., and Patel, A.J. (2018). Antifreeze protein hydration waters: Unstructured unless bound to ice. Proc. Natl. Acad. Sci. USA *115*, 8244–8246.

25. Ptitsyn, O.B. (1987). Protein folding: Hypotheses and experiments. J. Protein Chem. *6*, 273–293.

26. Delesky, E.A., Frazier, S.D., Wallat, J.D., Bannister, K.L., Heveran, C.M., and Srubar, W.V., 3rd (2019). Ice-Binding Protein from *Shewanella frigidimarinas* Inhibits Ice Crystal Growth in Highly Alkaline Solutions. Polymers (Basel) *11*, 299.

27. Chandra, S., and Aavik, J. (1987). Influence of proteins on some properties of portland cement mortar. Int. J. Cem. Compos. Lightweight Concr. *9*, 91–94.

28. Congdon, T., Notman, R., and Gibson, M.I. (2013). Antifreeze (glyco)protein mimetic behavior of poly(vinyl alcohol): detailed structure ice recrystallization inhibition activity study. Biomacromolecules *14*, 1578–1586.

29. Mitchell, D.E., Cameron, N.R., and Gibson, M.I. (2015). Rational, yet simple, design and synthesis of an antifreeze-protein inspired polymer for cellular cryopreservation. Chem. Commun. (Camb.) *51*, 12977–12980.

30. Hassan, C.M., and Peppas, N.A. (2000). Biopolymers, PVA Hydrogels, Anionic Polymerisation, Nanocomposites (Springer), pp. 37–65.

31. Lozinsky, V.I. (1998). Cryotropic gelation of poly(vinyl alcohol) solutions. Russ. Chem. Rev. *67*, 573–586.

32. Fouad, E.A., El-Badry, M., Neau, S.H., Alanazi, F.K., and Alsarra, I.A. (2011). Technology evaluation: Kollicoat IR. Expert Opin. Drug Deliv. *8*, 693–703.

33. Vance, T.D.R., Graham, L.A., and Davies, P.L. (2018). An ice-binding and tandem beta-sandwich domain-containing protein in Shewanella frigidimarina is a potential new type of ice adhesin. FEBS J. *285*, 1511–1527.

34. Mitchell, D.E., and Gibson, M.I. (2015). Latent Ice Recrystallization Inhibition Activity in Nonantifreeze Proteins: Ca^{2+}-Activated Plant Lectins and Cation-Activated Antimicrobial Peptides. Biomacromolecules *16*, 3411–3416.

35. Burkey, A.A., Riley, C.L., Wang, L.K., Hatridge, T.A., and Lynd, N.A. (2018). Understanding Poly(vinyl alcohol)-Mediated Ice Recrystallization Inhibition through Ice Adsorption Measurement and pH Effects. Biomacromolecules *19*, 248–255.

36. Weng, L., Stott, S.L., and Toner, M. (2018). Molecular Dynamics at the Interface between Ice and Poly(vinyl alcohol) and Ice Recrystallization Inhibition. Langmuir *34*, 5116–5123.

37. Naullage, P.M., Lupi, L., and Molinero, V. (2017). Molecular Recognition of Ice by Fully Flexible Molecules. J. Phys. Chem. C *121*, 26949–26957.

38. Kaufmann, J.P. (2004). Experimental identification of ice formation in small concrete pores. Cement Concr. Res. *34*, 1421–1427.

39. Setzer, M.J., Heine, P., Kasparek, S., Palecki, S., Auberg, R., Feldrappe, V., Siebel, E., Janssen, D.J., Auberg, R., et al. (2004). Test methods of frost resistance of concrete: GIF-Test: Capillary

suction, internal damage and freeze thaw test—Reference method and alternative methods A and B. Mater. Struct./Materiaux et Constructions *37*, 743–753.

40. Hover, K.C. (2006). Air content and density of hardened concrete in significance of tests and properties of concrete and concrete-making materials. In Significance of Tests and Properties of Concrete and Concrete-Making Materials, J. Lamond and J. Pielert, eds. (ASTM International), pp. 288–308.

41. Liu, Z., and Hansen, W. (2016). A geometrical model for void saturation in air-entrained concrete under continuous water exposure. Constr. Build. Mater. *124*, 475–484.

42. Gagné, R. (2016). Air entraining agents. In Science and Technology of Concrete Admixtures, P.-C. Aïtcin and R.J. Flatteds, eds. (Elsevier), pp. 379–391.

43. Chen, X., Wu, S., and Zhou, J. (2013). Influence of porosity on compressive and tensile strength of cement mortar. Constr. Build. Mater. *40*, 869–874.

44. Li, W., Pour-Ghaz, M., Castro, J., and Weiss, J. (2012). Water absorption and critical degree of saturation relating to freeze-thaw damage in concrete pavement joints. J. Mater. Civ. Eng. *24*, 299–307.

45. Fagerlund, G. (1977). The international cooperative test of the critical degree of saturation method of assessing the freeze/thaw resistance of concrete. Mater. Struct. *10*, 231–253.

46. Todak, H., Lucero, C., and Weiss, W.J. (2015). Why is the air there? Thinking about freeze-thaw in terms of saturation. Concrete InFocus *2015*, 3–7.

47. ASTM International (2019). C150/C150M-19a Standard Specification for Portland Cement (ASTM International).

48. Garnham, C.P., Gilbert, J.A., Hartman, C.P., Campbell, R.L., Laybourn-Parry, J., and Davies, P.L. (2008). A Ca2+-dependent bacterial antifreeze protein domain has a novel beta-helical ice-binding fold. Biochem. J. *411*, 171–180.

49. Knight, C.A., Hallett, J., and DeVries, A.L. (1988). Solute effects on ice recrystallization: an assessment technique. Cryobiology *25*, 55–60.

50. Ghods, P., Isgor, O.B., and Miller, T. (2009). The effect of concrete pore solution composition on the quality of passive oxide films on black steel reinforcement. Cement Concr. Compos. *31*, 2–11.

51. Inada, T., and Lu, S. (2004). Thermal hysteresis caused by non-equilibrium antifreeze activity of poly(vinyl alcohol). Chem. Phys. Lett. *394*, 361–365.

52. ASTM International (2019). C192/C192M-19 Standard Practice for Making and Curing Concrete Test Specimens in the Laboratory (ASTM International).

53. ASTM International (2018). C39/C39M-18 Standard Test Method for Compressive Strength of Cylindrical Concrete Specimens (ASTM International).

54. ASTM International (2019). C511-19 Standard Specification for Mixing Rooms, Moist Cabinets, Moist Rooms, and Water Storage Tanks Used in the Testing of Hydraulic Cements and Concretes (ASTM International).

55. ASTM International (2015). C666/C666M-15 Standard Test Method for Resistance of Concrete to Rapid Freezing and Thawing (ASTM International).

56. ASTM International (2019). C215-19 Standard Test Method for Fundamental Transverse, Longitudinal, and Torsional Resonant Frequencies of Concrete Specimens (ASTM International).

57. Mehta, P.K., and Monteiro, P.J.M. (2006). Concrete: Microstructure, Properties, and Materials (McGraw-Hill).

58. Batool, F., and Bindiganavile, V. (2017). Air-void size distribution of cement based foam and its effect on thermal conductivity. Constr. Build. Mater. *149*, 17–28.

59. Kim, K.Y., Yun, T.S., Choo, J., Kang, D.H., and Shin, H.S. (2012). Determination of air-void parameters of hardened cement-based materials using X-ray computed tomography. Constr. Build. Mater. *37*, 93–101.

Cell Reports Physical Science, Volume *1*

Supplemental Information

Inhibiting Freeze-Thaw Damage in Cement Paste and Concrete by Mimicking Nature's Antifreeze

Shane D. Frazier, Mohammad G. Matar, Jorge Osio-Norgaard, Anastasia N. Aday, Elizabeth A. Delesky, and Wil V. Srubar III

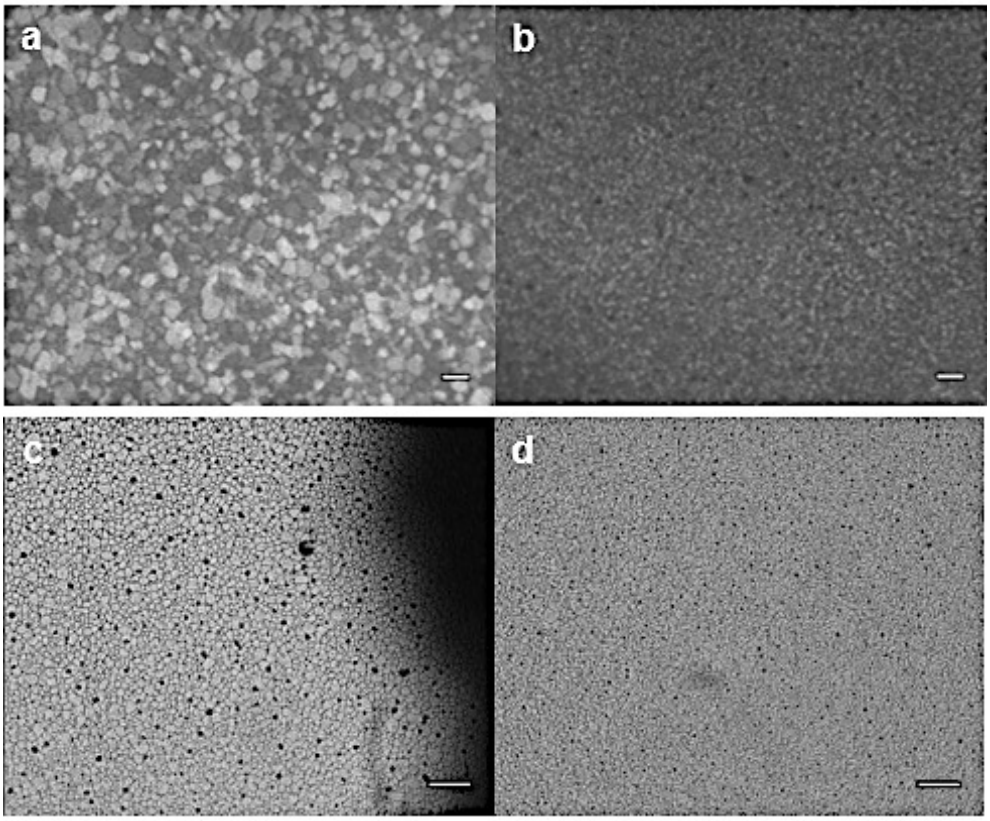

Figure S1. Optical micrographs of IRI splat assay of SfIBP and MpIBP in buffer solutions. Images show individual ice crystal grains that form in (a) SfIBP control buffer solution, (b) 0.125 mg/mL SfIBP in buffer solution, (c) MpIBP control buffer solution, (d) 0.10 mg/mL MpIBP in buffer solution after 30 minutes of annealing. Scale bars = 100 μm.

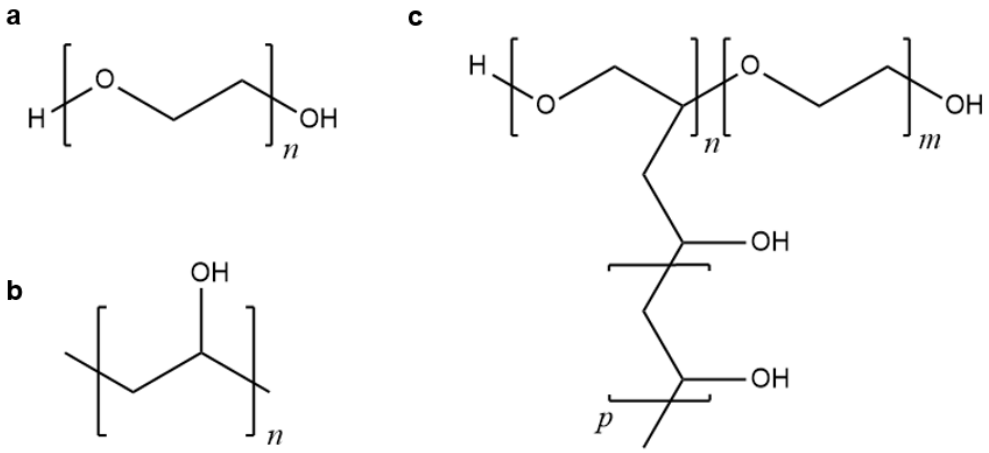

Figure S2. The chemical structure of polymers in this study. (**a**) polyethylene glycol (PEG) (**b**) polyvinyl alcohol (PVA) (**c**) polyvinyl alcohol-polyethylene glycol graft copolymer (PEG-PVA).

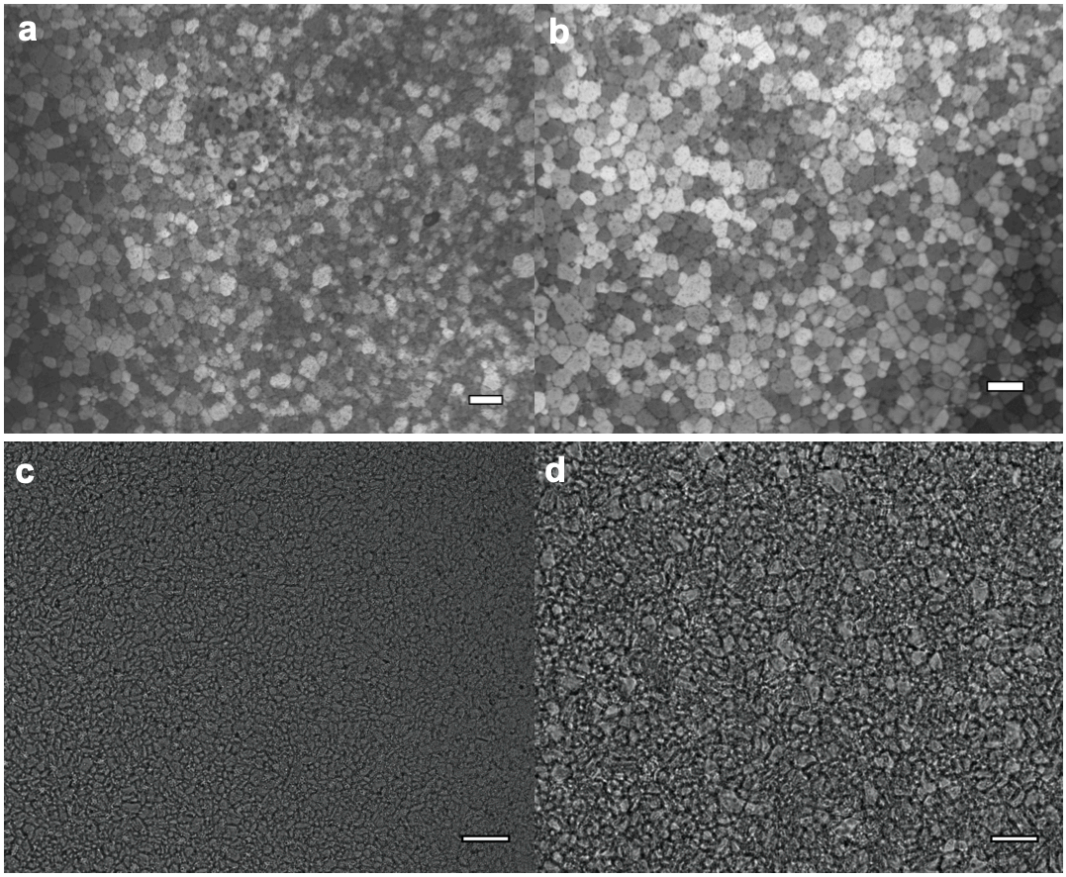

Figure S3. Optical micrographs of IRI splat assay of SfIBP and MpIBP in pH 13 adjusted buffer solutions. Images show individual ice crystal grains that form in (a) SfIBP control pH 13 adjusted buffer solution, (b) 0.125 mg/mL SfIBP in pH 13 adjusted buffer solution, (c) MpIBP control pH 13 adjusted buffer solution, (d) 0.10 mg/mL MpIBP in pH 13 buffer solution after 30 minutes of annealing. Scale bars = 100 μm.

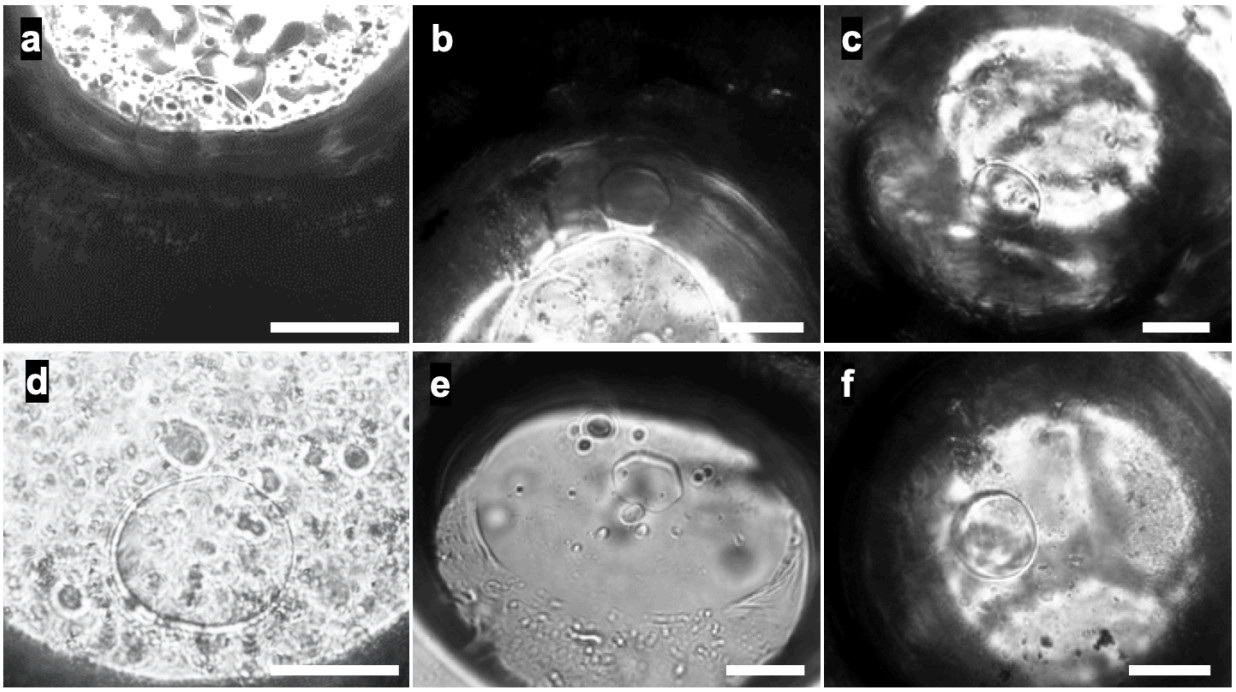

Figure S4. Optical micrographs of DIS for proteins. Single ice crystals for (**a**) SfIBP buffer solution, (**b**) 0.125 mg/mL SfIBP in buffer solution, (**c**) 0.125 mg/mL SfIBP in buffer solution saturated with $Ca(OH)_2$. (**d)** MpIBP buffer solution, (**e**) 0.10 mg/mL MpIBP in buffer solution, and (**f**) 0.10 mg/mL MpIBP in buffer solution saturated with $Ca(OH)_2$. Both SfIBP and MpIBP display hexagonal ice shaping in buffer solutions. Neither SfIBP or MbIBP maintain their ability to shape ice in the presence of saturated $Ca(OH)_2$ solution. Scale bars = 50 μm.

Table S1: Solution recipes for buffers used during MpIBP purification.

Buffer	Tris/HCl, pH 7.9	NaCl	$CaCl_2$	Glycerol	Imidazole
A	50 mM	0.5 M	2 mM	2% v/v	20 mM
B	50 mM	0.5 M	2 mM	2% v/v	40 mM
C	50 mM	0.5 M	2 mM	2% v/v	150 mM
D	50 mM	0.5 M	2 mM	2% v/v	200 mM
E	50 mM	50 mM	2 mM	-	-
F	50 mM	125 mM	2 mM	-	-
G	50 mM	0.5 M	2 mM	-	-
H	50 mM	1 M	2 mM	-	-
I	50 mM	1.25 M	2 mM	-	-
J	50 mM	1.5 M	2 mM	-	-
K	50 mM	2.5 M	2 mM	-	-

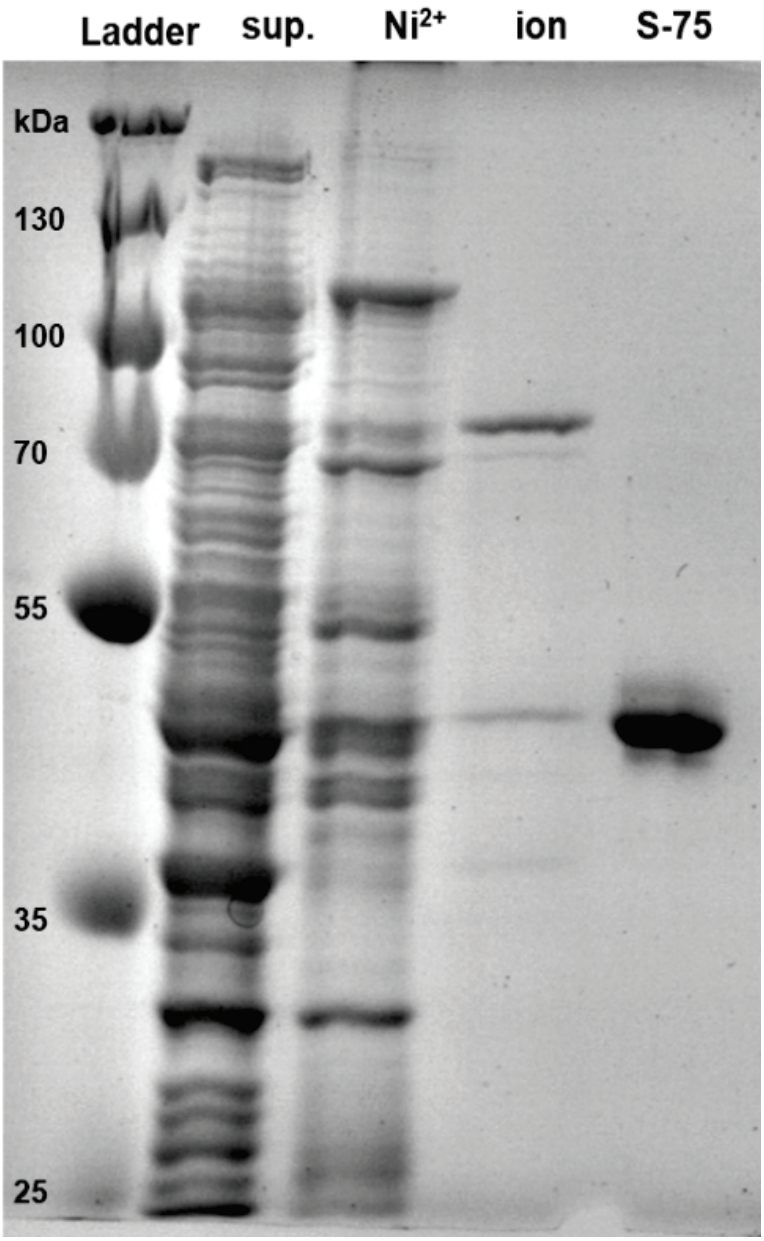

Figure S5. SDS-PAGE (10% w/v) analysis of the purification of MpIBP _RIV. Lanes from left to right are identified as follows: Ladder, DNA-ladder; sup., E. coli supernatant lysate; Ni^{2+}, pooled fractions from the Ni-NTA agarose affinity chromatography; ion, pooled fractions from the DEAE sepharose ion-exchange chromatography; S-75, pooled fractions from the size-exclusion chromatography on a HiLoad Superdex 75.

Table S2: Composition of protein samples tested for IRI activity.

	Buffer Solution Constituents	**pH 13 Adjusted Buffer Solution Constituents**
0.125 mg/mL SfIBP	20 mM Tris	20 mM Tris* 168.5 mM 0.007 mM Ca^{2+} 23.9 mM Na^{+} 37.3 mM K^{+} 20.6 mM S^{2-}
0.10 mg/mL MpIBP	10 mM Tris 15 mM NaCl 10 mM $CaCl_2$ 18 mM HCl	10 mM Tris 15 mM NaCl 10 mM $CaCl_2$ 58 mM NaOH

* Solution was prepared as described in Delesky *et al*.[25]

Table S3. Chemical Composition of Type I/II OPC

Composition	Percentage
Al_2O_3	4.38
CaO	62
Fe_2O_3	3.33
K_2O	0.757
MgO	1.38
MnO	0.21
Na_2O	0.19
P_2O_5	0.183
SiO_2	19.7
SO_3	3.32
TiO_2	0.18
LOI	2.96

Table S4. Sieve analysis of fine and coarse aggregates according to ASTM C136[2] & C117[3].

Sieve Size		Percent Passing (%)
1”	25.0 mm	100
¾”	19.0 mm	90
½”	12.5 mm	35
3/8”	9.5 mm	20
No. 4	4.75 mm	3
No. 8	2.36 mm	2
No. 16	1.18 mm	1
No. 30	600 µm	1
No. 50	300 µm	1
No. 100	150 µm	1
No. 200	75 µm	1.3

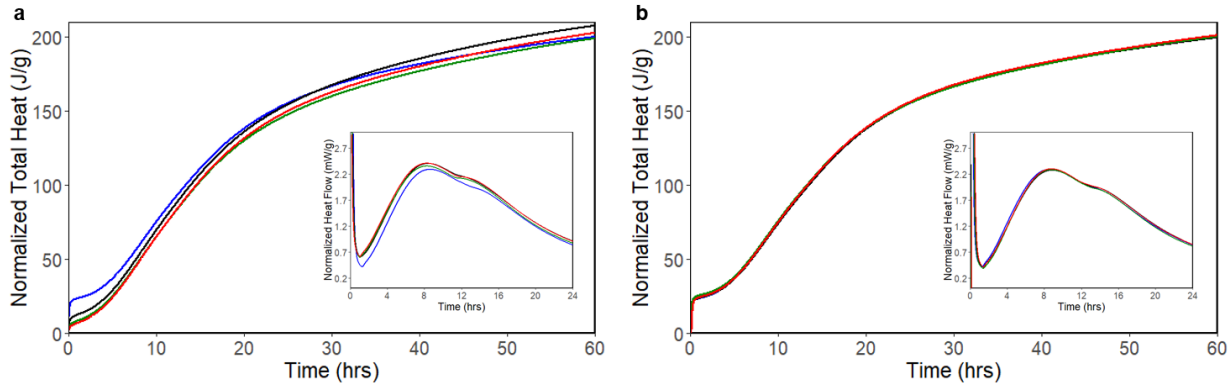

Figure S6. Isothermal conduction calorimetry curves. Normalized total heat plots for (**a**) low concentrations: control (blue), PEG-L (black), PVA-L (green), PEG-PVA-L (red) and (**b**) high concentrations: control (blue), PEG-H (black), PVA-H (green), PEG-PVA-H (red). Inset images are normalized heat flow.

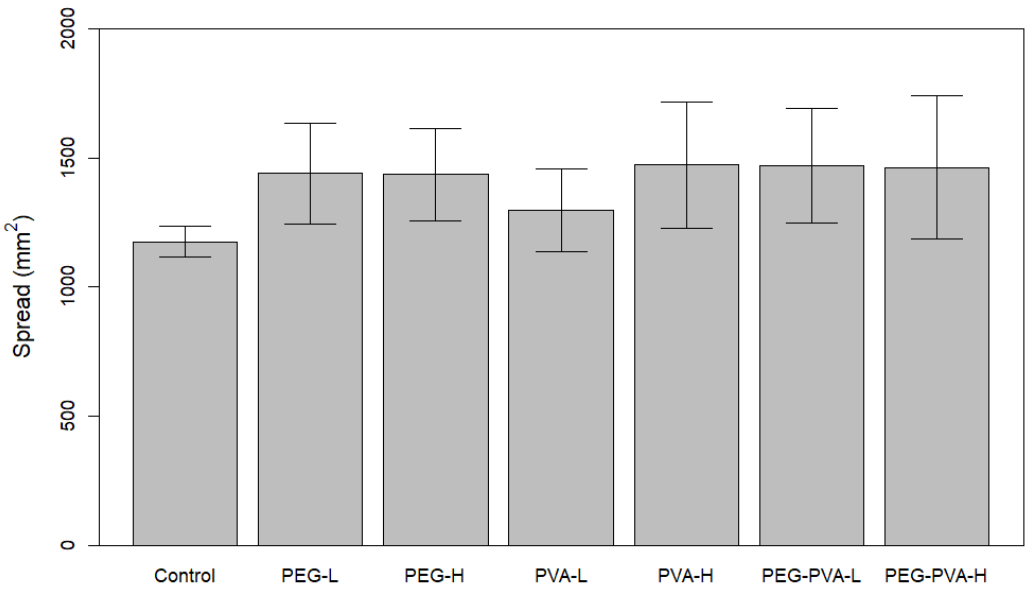

Figure S7. Flowability (mini slump cone) results for all samples at t = 0. Values presented are the average and one standard deviation of three replicates.

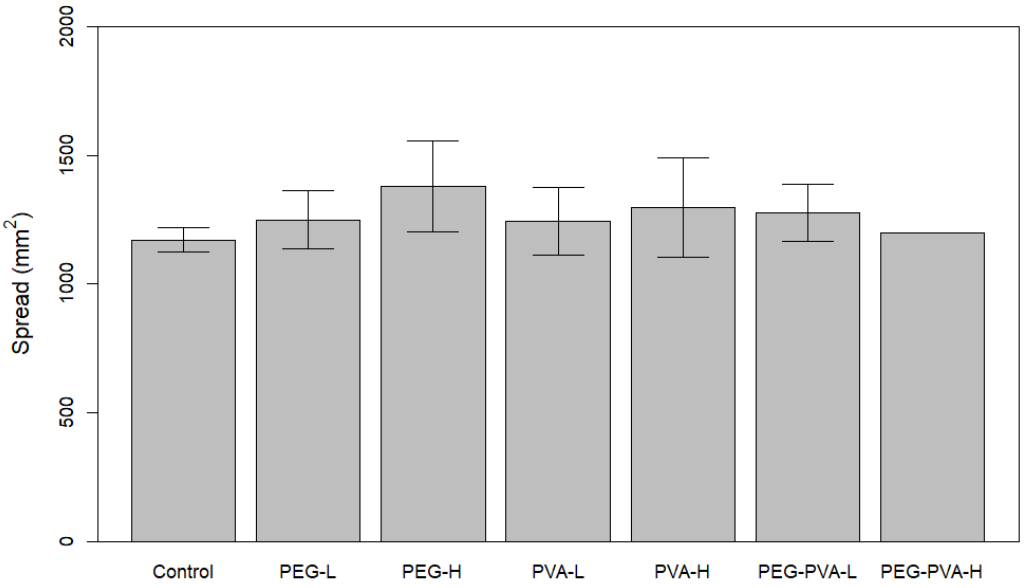

Figure S8. Flowability (mini slump cone) results for all sample at t = 60 mins. Values presented are the average and one standard deviation of three replicates.

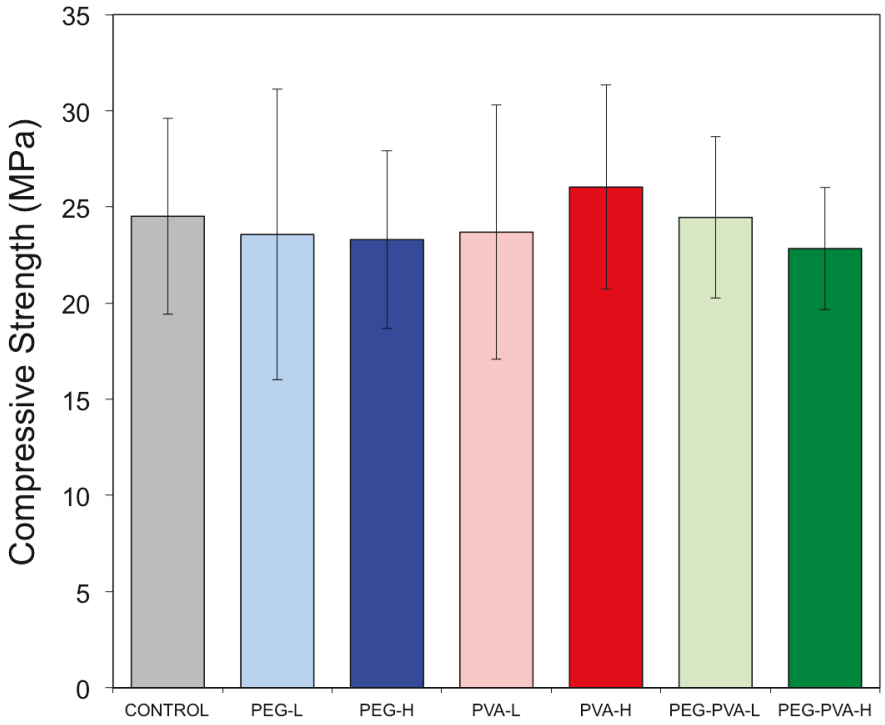

Figure S9. Initial compressive strength results of all paste formulations. Compressive strength of all samples with one standard deviation reported for six results (n = 6).

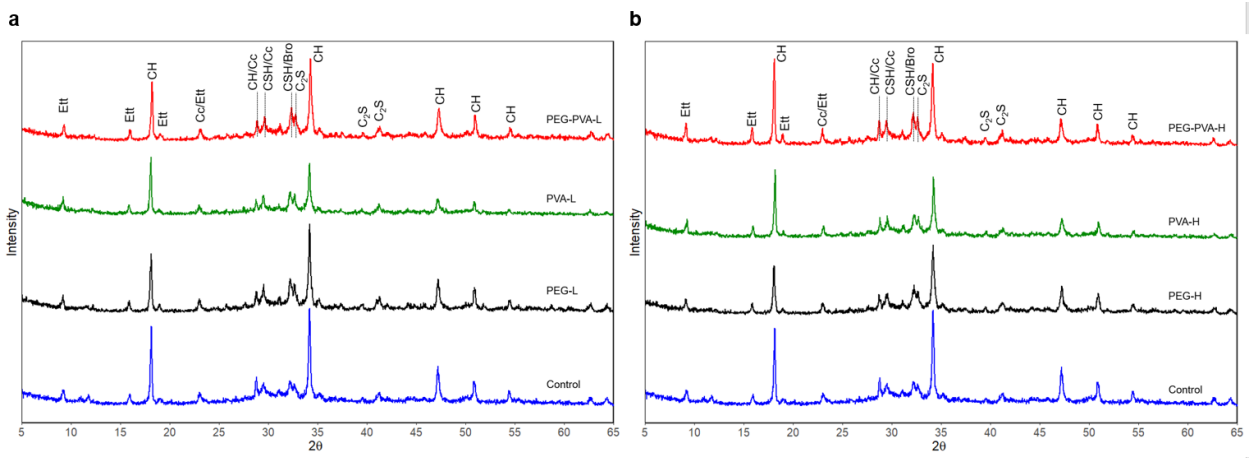

Figure S10. XRD diffractograms of samples after 14-day cure. Diffractograms of OPC control and (**a**) low concentration polymer additions and (**b**) high concentration polymer additions. Bro: Brownmillerite; Cc: calcite; CH: portlandite; CSH: calcium silicate hydrate; Ett: Ettringite; C_2S: Larnite (Belite).

Table S5: Summary of peaks identified in XRD diffractograms.

Symbol	Mineral	2θ	Reference
Bro	Brownmillerite	32.1	12
Cc	Calcite	23, 29.3	12,13,14
CH	Portlandite	18.1, 29, 34.1, 47.2, 51, 54.5	12,13,14,15,16
CSH	Calcium silicate hydrate	29.6, 32.2	14,17
C_2S	Larnite (Belite)	32.2, 32.6, 39.5, 41.2	12,18
Ett	Ettringite	9.1, 15.8, 23	12,13,14,15,16

Table S6. Summary of MXCT 3D reconstruction air void analysis. The total number of air voids, maximum air void size, and minimum air void size for each sample scan are reported.

Sample	Total number of voids in scanned volume	Maximum void diameter (µm)	Minimum void diameter (µm)
Control 1	2771	874.36	49.89
Control 2	4150	748.99	49.89
PEG-L 1	3472	821.23	49.89
PEG-L 2	3276	575.88	49.89
PEG-H 1	546	1,381.44	49.89
PEG-H 2	5121	914.16	49.89
PVA-L 1	3194	857.38	49.89
PVA-L 2	2781	882.61	49.89
PVA-H 1	1761	748.99	49.89
PVA-H 2	3373	687.31	49.89
PEG-PVA-L 1	1336	611.97	49.89
PEG-PVA-L 2	4045	971.44	49.89
PEG-PVA-H 1	4631	943.67	49.89
PEG-PVA-H 2	3356	830.57	49.89

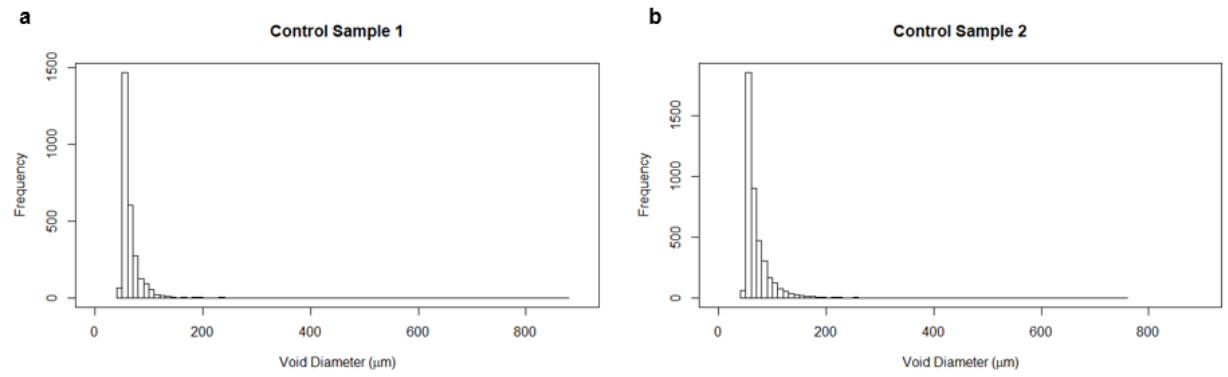

Figure S11. Histogram of void diameters for (**a**) control sample 1 and (**b**) control sample 2.

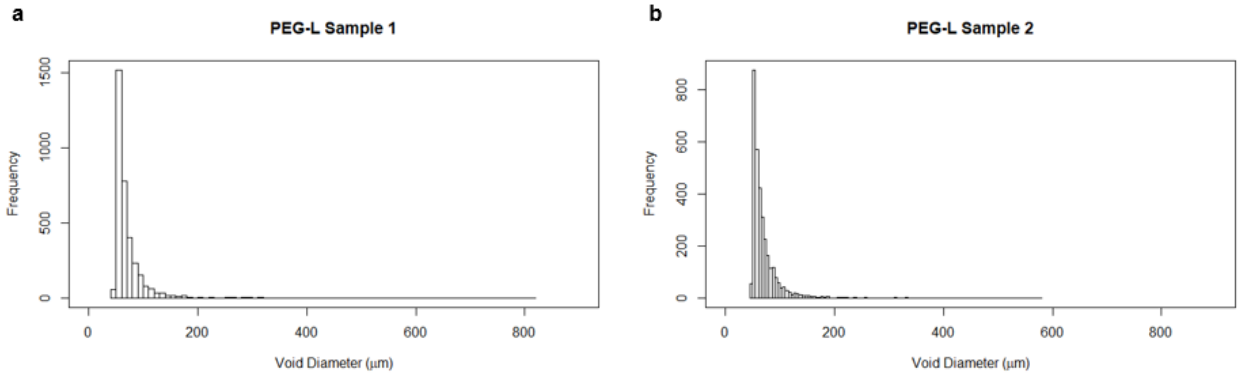

Figure S12. Histogram of void diameters for (**a**) PEG-L sample 1 and (**b**) PEG-L sample 2.

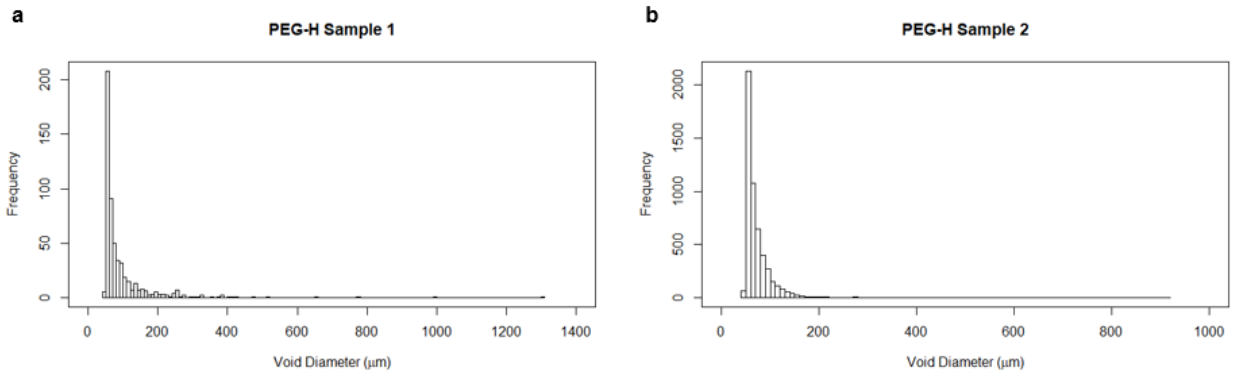

Figure S13. Histogram of void diameters for (**a**) PEG-H sample 1 and (**b**) PEG-H sample 2.

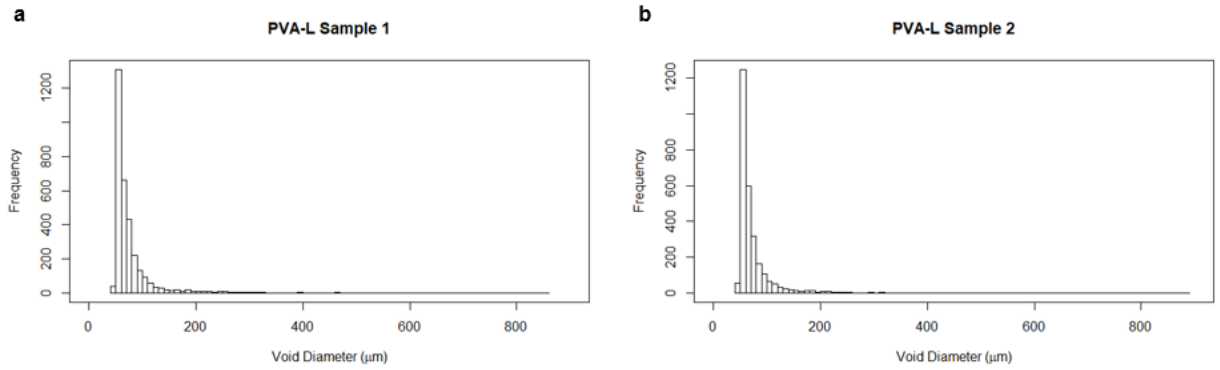

Figure S14. Histogram of void diameters for (**a**) PVA-L sample 1 and (**b**) PVA-L sample 2.

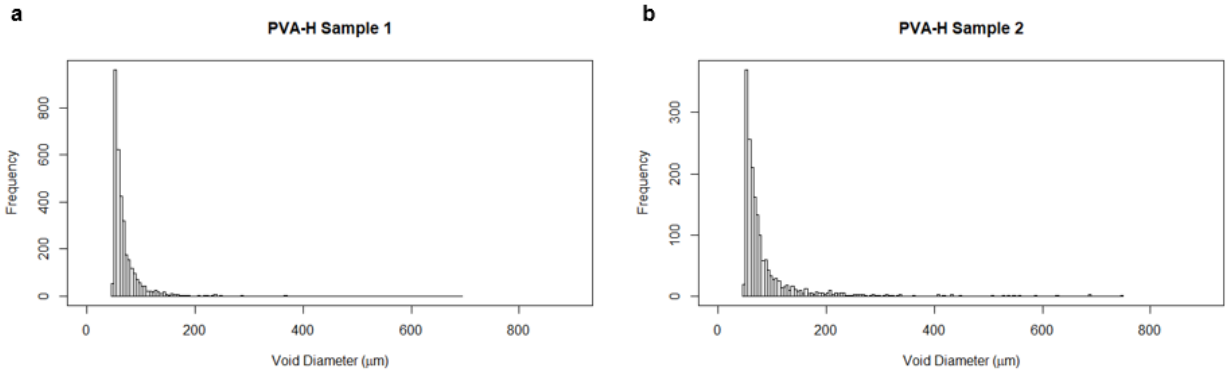

Figure S15. Histogram of void diameters for (**a**) PVA-H sample 1 and (**b**) PVA-H sample 2.

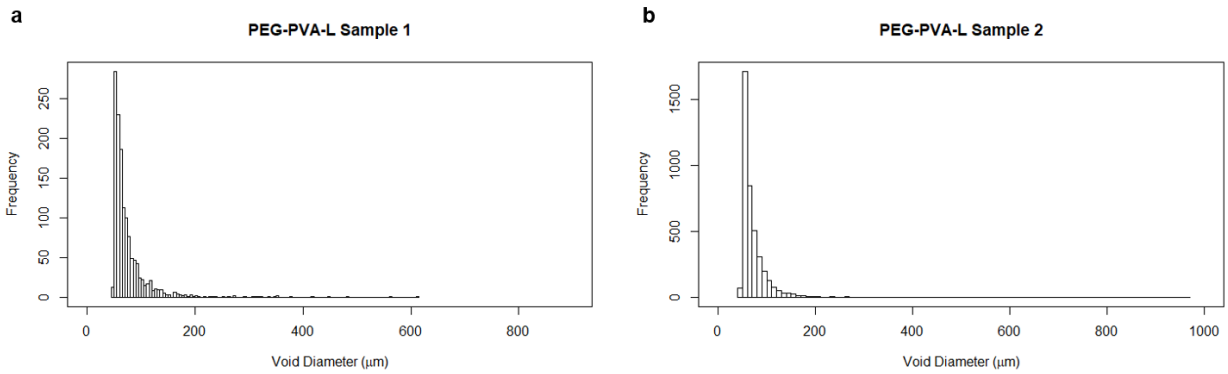

Figure S16. Histogram of void diameters for (**a**) PEG-PVA-L sample 1 and (**b**) PEG-PVA-L sample 2.

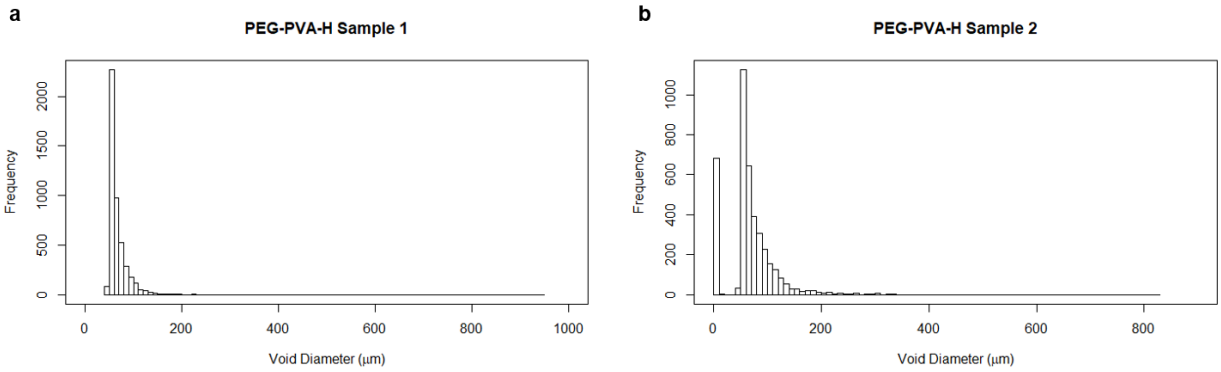

Figure S17. Histogram of void diameters for (**a**) PEG-PVA-H sample 1 and (**b**) PEG-PVA-H sample 2.

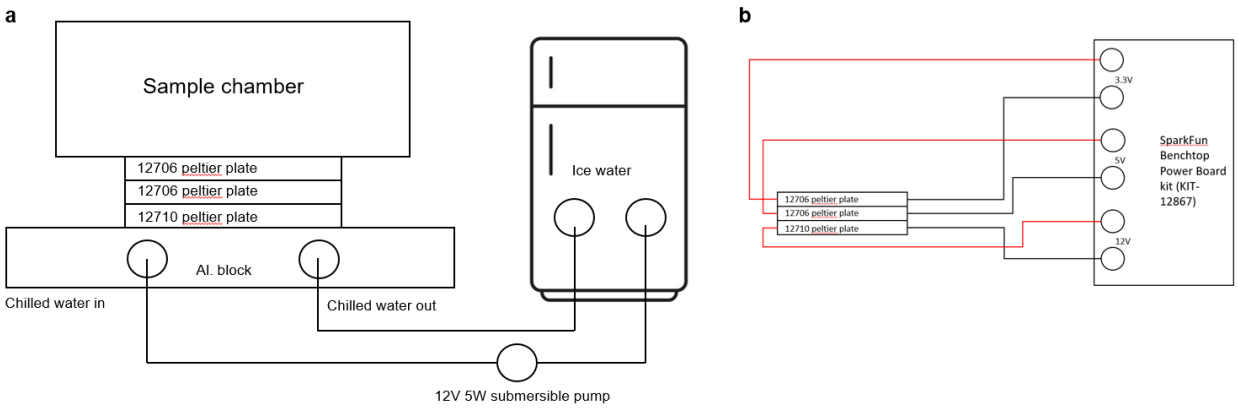

Figure S18. Layout of custom-built freeze-thaw chamber used in study. (**a**) Schematic diagram of the freeze-thaw chamber and (**b**) wiring diagram of Peltier plates to 12V, 5V, and 3.3V power supply.

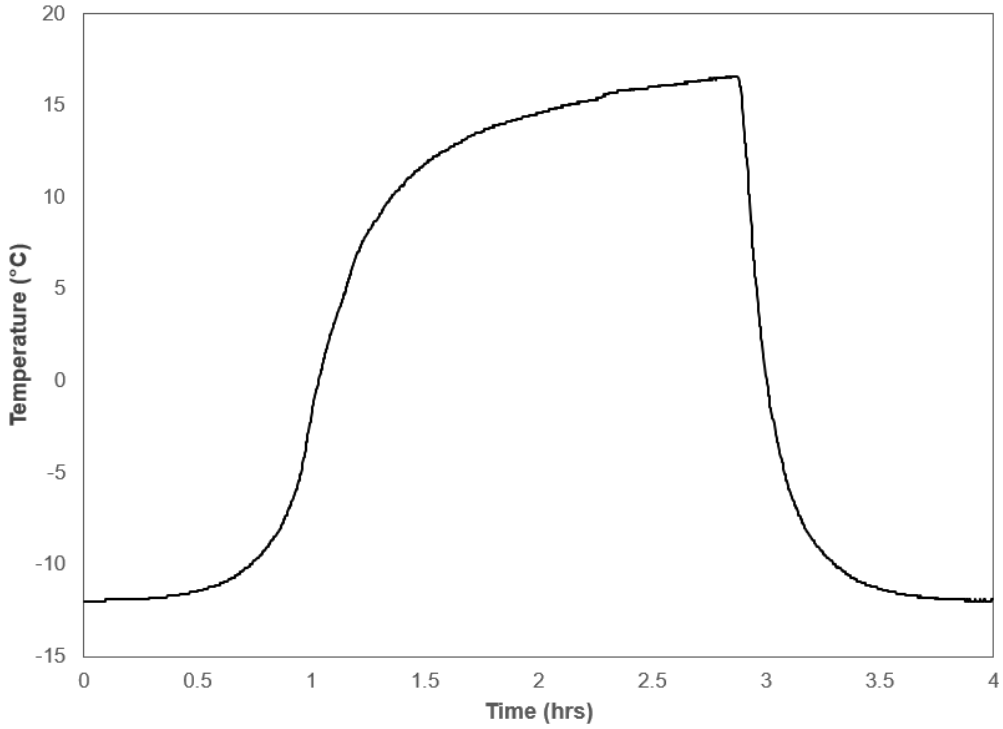

Figure S19. Temperature profile of freeze-thaw chamber for cement paste. The temperature profile showing the maximum and minimum temperatures, rate of heating and cooling, and length of a single cycle.

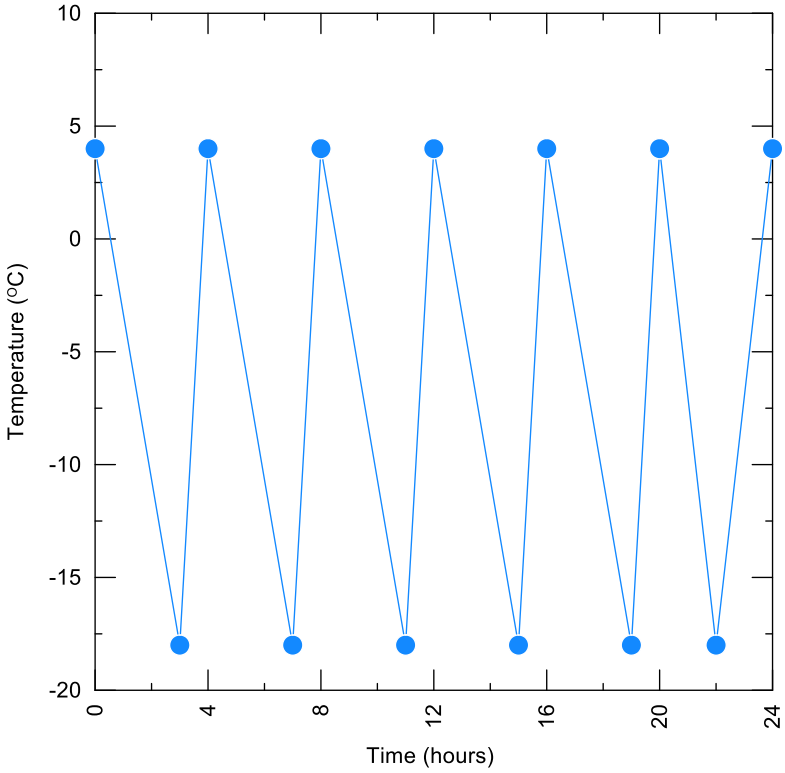

Figure S20. Temperature profile of the freeze-thaw temperature used in the study.

Table S7. Fresh state slump of each concrete mixture formulation.

Test Group	Slump (mm)
Control	9.5
0.022%	35.7
0.066%	41.3
0.25%	63.5
1%	165.1
AEA (Air Entrained)	15.9

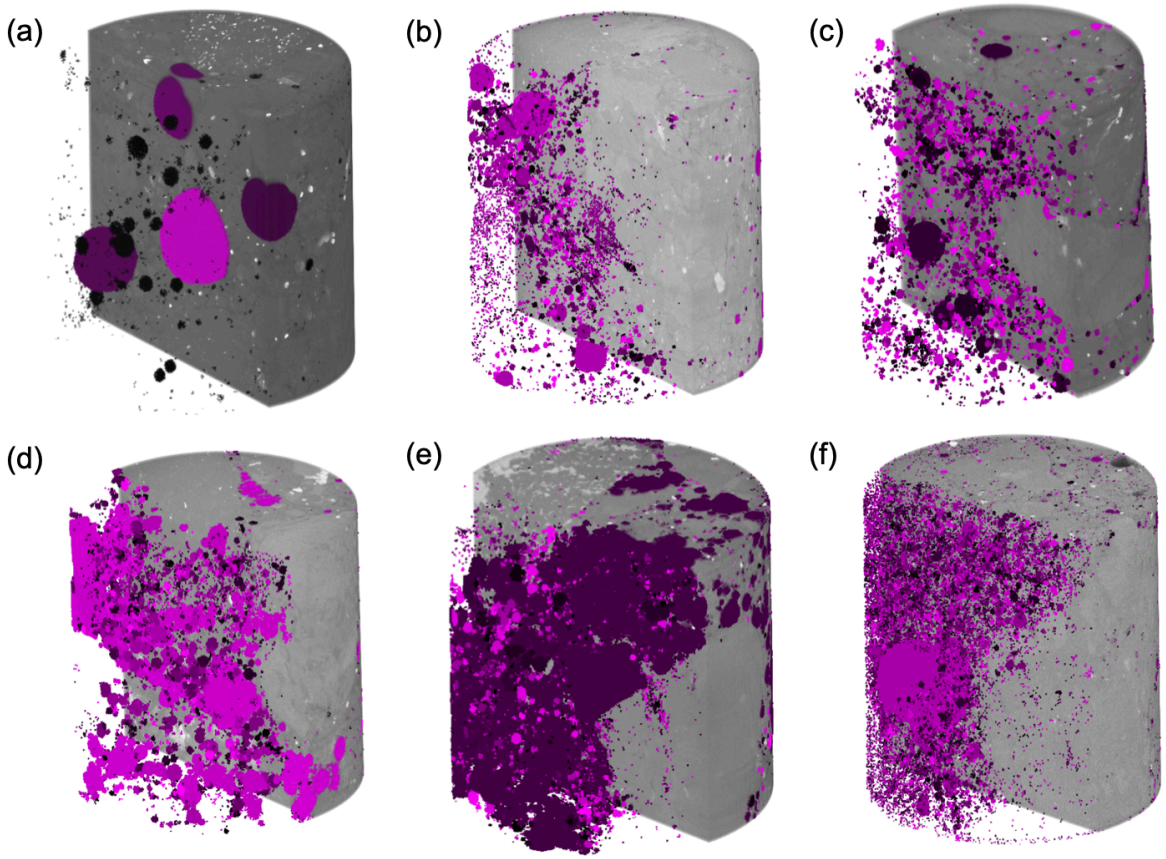

Figure S21. MXCT 3D reconstructions of air void system for each concrete test group. Representative 3D reconstructions with air voids highlighted in pink and purple for (**a**) control, (**b**) 0.022%, (**c**) 0.066%, (**d**) 0.25%, (**e**) 1.0%, and (**f**) AEA test groups. Each cylindrical scanned volume is ~ 9.6 mm in diameter and 11 mm in height.

Table S8. Hardened state concrete air void parameters.

Test Group	Number of Air Voids	Specific Surface (mm^2/mm^3)	Voids / Unit Volume (mm^{-3})
Control	1.24×10^5	8.94	123
0.022%	3.39×10^5	32.08	365
0.066%	6.44×10^5	28.19	668
0.25%	4.63×10^5	17.95	513
1.0%	3.86×10^5	11.76	422
AEA	1.21×10^6	35.61	1267

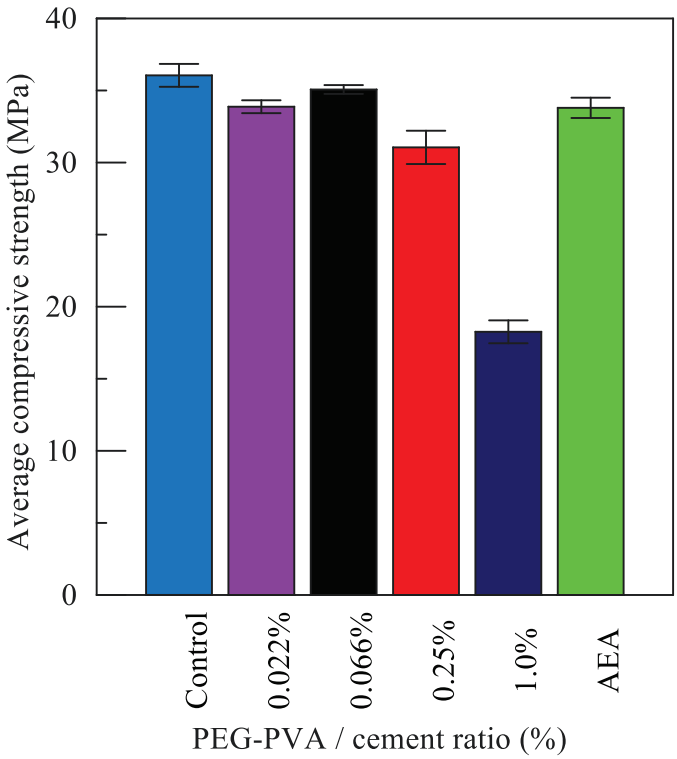

Figure S22. Average compressive strength of each test group. Compressive strength determined on cylindrical specimen with no exposure to freeze-thaw cycling. Error bars represent one standard deviation of n=3 replicates.

Supplemental Experimental Procedures

Marinomonas primoryensis Antifreeze Protein (MpIBP) Expression and Purification

Expression of MpIBP was adapted from Garnham et al.[1] Briefly, positive clones with MpIBP were grown overnight (37 °C, 200 rpm) and used to seed an agar plate with kanamycin (100 μg/mL). Positive colonies were used to inoculate 1.6 L of Luria-Bertani medium with kanamycin (100 μg/mL) and grown at 37 °C and 200 rpm until OD600 reached 0.5. The temperature was then lowered to 23 °C and cells were allowed to grow until OD600 = 1 (~2 hours), then isopropyl β-D-1-thiogalactopyranoside was added to a final concentration of 1 mM to induce expression overnight at 23 °C. Cells were recovered by centrifugation for 30 min at 4,300 g and 4 °C. Cells were resuspended in Buffer A (**Table S1**). The resuspension was sonicated using a Qsonica Q55 Sonicator Ultrasonic Homogenizer with Probe 55W (5x, 45 seconds, 50% amplitude) to break open the cells. Cellular debris was removed *via* centrifugation (1.5 hours, 4 °C, 4,300 g).

To purify MpIBP, the crude cellular lysate was mixed with 16 mL of Ni-NTA (Ni^{2+}-nitriloacetate) resin and stirred at 4 °C overnight. The lysate-Ni-NTA mixture was loaded into a column and washed with Buffers A through C, and eluted with Buffers D and E (**Table S1**). Fractions were examined using SDS-PAGE, and samples displaying bands for MpIBP (~44kD) were pooled. To remove small protein contaminants and reduce salt content, pooled fractions were run through a ThermoScientific Protein Biology 50 mL 30kD Pierce Protein Concentrator (2000g, 4 °C) in Buffer F (10-fold reduction, 3x). The concentrate was loaded onto a DEAE–Sepharose resin column equilibrated with Buffer F. The column was washed with Buffers F through H, and protein was eluted with Buffers I through K (**Table S1**). Fractions were run using

SDS-PAGE, and samples displaying a ~44 kDa MW band were pooled and concentrated. Protein concentrate was then run using a GE Healthcare AKTApurifier FPLC with a Frac 950 equipped with a HiLoad Superdex 75 pg preparative size exclusion chromatography column. Fractions that displayed absorbance were run using SDS-PAGE to determine MpIBP containing fractions, which were again pooled and concentrated. Concentrate purity was verified using SDS-PAGE **Figure S5**, and concentration was determined using UV-Vis.

Sodium-dodecyl sulfate polyacrylamide gel electrophoresis (SDS-PAGE)

Sodium-dodecyl sulfate polyacrylamide gel electrophoresis (SDS-PAGE) was performed on MpIBP to determine sample purity. MpIBP samples were denatured prior to SDS-PAGE using 2-mercaptoethanol and subsequent heating (95°C, 10 minutes). Samples were loaded onto a 10% denaturing acrylamide gel (1.0 mm × 15 well; 70 min, 150 V, 300 mA, 1X Tris-Glycine-SDS PAGE running buffer, pH 8.8) and compared to a 10-250 kDa PageRuler Plus protein ladder (ThermoFisher Scientific) to estimate molecular weight. MpIBP content within the gel was stained using Coomassie SimplyBlue SafeStain (Invitrogen) according to manufacturer specifications.

Chemical Composition of Cement & Sieve Analysis of Aggregate

Quantitative X-Ray Fluorescence (XRF) was performed on Type I/II OPC used in this study to determine the chemical composition. The XRF results, including oxide content, can be found in **Table S3**. Size analysis of coarse aggregate is shown in **Table S4**.

Fresh-State Properties of Cement Paste

Isothermal Conduction Calorimetry

Isothermal conduction calorimetry (ICC) was performed to understand the impact of the polymeric admixtures on both the heat of hydration and time of set. A TAM Air 8-Channel Isothermal Calorimeter from TA instruments was set at 21°C and allowed to equilibrate for 24 hours. All samples were mixed for 3 minutes in glass ICC vials, with a water to cement (w/c) ratio of 0.5, and immediately placed in the calorimeter and allowed to equilibrate for 1 hour before the calorimeter signal was considered stable. Data was measured for 72 hours to capture the peak thermal power. The peak thermal power at 50% was used to approximate time of set.[4]

ICC results in **Figure S6** show that time of set and heat of hydration were minimally impacted at low concentrations of polymer, whereas no change was observed in high concentration of polymer. **Figure S6 (a)** shows that the addition of PEG-L results in slightly higher total heat compared to the control and all other polymer additions. The inset shows that for all polymer additions at low concentrations there is a marginal acceleration in hydration. **Figure S6 (b)** shows no difference in total hydration or total heat for high-concentrations polymer additions compared to the control. Generally, the addition of water-soluble polymers reduces heat of hydration and retards set, however this behavior is typically observed when the polymeric additions are ≥0.1% by weight of cement.[5] Many polymeric materials help to impede flocculation of cement grains, including PVA, which can result in accelerated hydration.[6,7] This ability is dependent on polymer concentration. However, the high concentrations in this study appear to not retard time of set.

Flowability

To test the flowability of cement pastes, a mini slump cone test was performed.[8] Samples were prepared as outlined in materials and methods using a w/c of 0.42. After mixing the miniature slump cone was filled approximately one-third of the way and tamped no more than 25 times to remove entrapped air. This procedure was repeated twice more to fill the cone. Finally, the top of the cone was screeded. The cone was removed from the sample and the diameter of the base (at two locations) was measured immediately and at 5 mins, 15 mins, 30 mins, 45 mins, 60 mins, and 24 hours. The diameter was used to calculate the average spread area at each time point. Each mixture composition was tested in triplicate.

All polymers increased the fluidity when compared to the control. The initial areas are shown in **Figure S7** and after 60 minutes in **Figure S8**. The initial areas increased up to 25% (PVA-H, PEG-PVA-L) and, after 60 minutes, up to 17% (PEG-H).

Hardened-State Properties of Cement Paste

Compressive strength

Initial compressive strengths of all samples, **Figure S9**, show that there are no significant effects due to polymer addition, regardless of concentration. These results further indicate that minimal air was entrained, given that air entrainment is well known to decrease compressive strength by ~ 5% per 1% entrained air.[9] Previous research has shown that higher additions of PEG and PVA (0.1 to 3 wt.% of cement) can lead to denser microstructures and increased compressive strength by retarding flocculation during hydration, thereby enabling higher reactivity of cement particles.[10,11] However, the low wt.% additions investigated herein neither increased nor decreased the compressive strength of the paste.

Mineralogy

X-ray diffraction (XRD) was performed on all samples to qualitatively determine mineralogy. Samples for all mixtures were crushed into a fine powder and suspended in ethanol (200 proof) to homogenize the powder. The suspension was pipetted onto a silica zero background plate and placed on a heated plate to allow for ethanol evaporation resulting in a thin film of sample. XRD patterns were collected using a Siemens D500 equipped with a Cu Kα radiation source. Data were recorded in the range of $2\theta = 5°$ to 65° with a step size of 0.02° and a dwell time of 2 sec/step.

Figure S10 (a) and Figure S10 (b) show XRD diffractograms for low and high concentration polymer additions respectively. Regardless of polymer concentration the main constituent minerals (portlandite, calcite, and calcium silicate hydrate) are present. Additionally, ettringite, brownmillerite, and larnite (belite) were present in all samples. The presence of these minerals in hardened ordinary portland cement paste was expected.[12] **Table S5** summarizes the peaks identified in **Figure S10** and the corresponding mineral.

Air Content

As described in the materials and methods section, the volume percent of air, or air content, in samples pre-freeze-thaw cycling was determined from the volume of all voids with diameters > 50 μm ($V_{>50}$). Voids were identified from 3D reconstructions of MXCT scans. Dragonfly 3.1 software (Object Research Systems) was used to generate the reconstructions and calculate the scanned volume of sample (V_{sample}), and $V_{>50}$. **Table S6** provides the number of voids in the scanned volume, maximum void diameter, and minimum void diameter of each sample analyzed. **Figures S11-S17** provide histograms of the observed void diameters. Note that no void was

found to be greater than 1 mm in diameter, with the exception of one present in PEG-H sample 1. Although this void was larger than 1 mm, which is generally considered the upper threshold for entrained air diameter, it was quite spherical and, therefore, was still considered to be *entrained* air and not *entrapped* air (data not shown).

Freeze-thaw Chamber for Cement Paste

A schematic of the custom-built freeze-thaw chamber can be found in **Figure S18 (a)**. All parts used to make the chamber were commercially available. The sample chamber was 3-in x 3-in x 1.5-in (L x W x H). Ice water was kept cold in a refrigerator and pumped through an aluminum block to act as a heat sink for stacked Peltier plates, which provided the source for cold temperatures. The Peltier plates were stacked and wired to a benchtop power board (SparkFun), as shown in **Figure S18 (b)**, to achieve the desired cooling temperature. The temperature within the chamber was monitored with a DHT-22 temperature sensor (SparkFun). The temperature sensor was connected to a Raspberry Pi Zero W for data collection. The temperature profile can be found in **Figure S19**.

Temperature Profile of Freeze-Thaw Chamber Used for Concrete

Figure S20 provides the temperature profile of the freeze-thaw chamber used in the study. The temperature reached -18°C in three hours during the freeze cycles. The temperature reached 4°C in one hour during the thaw cycle. The observed variation was ± 2°C.

Fresh- and Hardened-State Properties of Concrete

Table S7 provides the observed slump values for each concrete test group. The results show that as the amount of PEG-PVA increases a larger slump is observed. For the additions chosen in this study the relationship between PEG-PVA addition and slump is proportional. An increase in slump has previously been observed with PVA addition.[19,20] In fact, the observed slump value for 1% addition in this study agrees well with that reported by J.-H. Kim, et al. [20].

Air Void Distribution

The air void distribution can be found in **Figure S21 (a)**. It is clear that for all test groups the majority of identified voids had a diameter between 16 μm and 100 μm. However, for the control, 0.25%, 1.0%, and AEA test groups the largest portion of overall air void volume is from air voids with diameters greater than 1000 μm as shown in **Figure S21 (b)**. The 0.022% and 0.066% test groups have a fairly well distributed percentage of volume contributed by each size range of air voids. The AEA test group stabilized the largest number of air voids by nearly a factor of 10 as shown in **Table S8**.

Compressive Strength

Initial average compressive strengths of all samples, **Figure S22**, show that there are no significant effects due to polymer addition, regardless of concentration. It was found that the compressive strength of concrete with PEG-PVA at additions of 0.022% and 0.066% all fall within one standard deviation of the average compressive strength of the control indicating that there is no significant effect of PEG-PVA addition at these dosages. Samples containing AEA also showed no significant reduction in compressive strength. Although it is common to observe reductions in compressive strength with AEA addition, in a research setting it is possible to

minimally affect the strength depending on the type of AEA and dosage.[21,22] On the other hand, specimens with PEG-PVA at additions of 0.25% and 1.0% have shown a significant reduction in strength likely due to the relatively large air contents.

SUPPLEMENTAL REFERENCES

1. C. P. Garnham, J. A. Gilbert, C. P. Hartman, R. L. Campbell, J. Laybourn-Parry, P. L. Davies, A Ca2+-dependent bacterial antifreeze protein domain has a novel beta-helical ice-binding fold. *Biochem J.* **411**, 171-180 (2008).

2. ASTM International. C136/C136M-19 Standard Test Method for Sieve Analysis of Fine and Coarse Aggregates. West Conshohocken, PA; ASTM International, 2019.

3. ASTM International. C117-17 Standard Test Method for Materials Finer than 75-μm (No. 200) Sieve in Mineral Aggregates by Washing. West Conshohocken, PA; ASTM International, 2017.

4.ASTM International. C1679-17 Standard Practice for Measuring Hydration Kinetics of Hydraulic Cementitious Mixtures Using Isothermal Calorimetry. West Conshohocken, PA; ASTM International, 2017.

5. N. Roussel, A. Lemaître, R. J. Flatt, P. Coussot, Steady state flow of cement suspensions: A micromechanical state of the art. *Cement and Concrete Research* **40**, 77-84 (2010).

6. A. Zingg, L. Holzer, A. Kaech, F. Winnefeld, J. Pakusch, S. Becker, L. Gauckler, The microstructure of dispersed and non-dispersed fresh cement pastes — New insight by cryo-microscopy. *Cement and Concrete Research* **38**, 522-529 (2008).

7. N. B. Singh, S. Rai, Effect of polyvinyl alcohol on the hydration of cement with rice husk ash. *Cement and Concrete Research* **31**, 239-243 (2001).

8. P. Wedding, D. Kantro, Influence of Water-Reducing Admixtures on Properties of Cement Paste—A Miniature Slump Test. *Cement, Concrete, and Aggregates* **2**, 95-102 (1980).

9. Mehta, P. Kumar, Monteiro, Paulo J. M., Concrete: Microstructure, Properties, and Materials (McGraw-Hill, 2006).

10. C. C. Thong, D. C. L. Teo, C. K. Ng, Application of polyvinyl alcohol (PVA) in cement-based composite materials: A review of its engineering properties and microstructure behavior

Constr. Build. Mater. **107**, 172-180 (2016).
11. V. K. Singh, S. D. Khatri, R. K. Singh, Hydration and Some Other Properties of Polyethylene Glycol Modified Cement Products *Trans. Indian Ceram. Soc*. **61**, 152-161 (2002).
12. C. Alonso, L. Fernandez, Dehydration and rehydration processes of cement paste exposed to high temperature environments. *Journal of Materials Science* **39**, 3015-3024 (2004).
13. M. Castellote, L. Fernandez, C. Andrade, C. Alonso, Chemical changes and phase analysis of OPC pastes carbonated at different CO2 concentrations. *Materials and Structures* **42**, 515-525 (2009).
14. R. Snellings, in *A Practical Guide to Microstructural Analysis of Cementitious Materials,* K. Scrivener, R. Snellings, B. Lothenbach, Eds. (CRC Press, 2015), chap. 4, pp. 108-162.
15. T. Ramlochan, P. Zacarias, M. D. A. Thomas, R. D. Hooton, The effect of pozzolans and slag on the expansion of mortars cured at elevated temperature. *Cement and Concrete Research* **33**, 807-814 (2003).
16. A. Bertron, J. Duchesne, G. Escadeillas, Degradation of cement pastes by organic acids. *Materials and Structures* **40**, 341-354 (2007).
17. J. Schneider, M. A. Cincotto, H. Panepucci, 29Si and 27Al high-resolution NMR characterization of calcium silicate hydrate phases in activated blast-furnace slag pastes. *Cement and Concrete Research* **31**, 993-1001 (2001).
18. A. Mendes, W. P. Gates, J. G. Sanjayan, F. Collins, NMR, XRD, IR and synchrotron NEXAFS spectroscopic studies of OPC and OPC/slag cement paste hydrates. *Materials and Structures* **44**, 1773-1791 (2011).
19. C.C. Thong, D.C.L. Teo, C.K. Ng, Application of polyvinyl alcohol (PVA) in cement-based composite materials: A review of its engineering properties and microstructure behavior *Construction and Building Materials* **107**, 172–180 (2016).

20. J.-H. Kim, R.E. Robertson, A.E. Naaman, Structure and properties of poly(vinyl alcohol)-modified mortar and concrete *Cement and Concrete Research* **29**, 407–415 (1999).

21. X. Ouyang, Y. Guo, X. Qiu, The feasibility of synthetic surfactant as an air entraining agent for the cement matrix. *Construction and Building Materials* **22**, 1774-1779 (2008).

22. J. Chen, M. Qiao, N. Gao, Q. Ran, J. Wu, G. Shan, S. Qi, S. Wu, Cationic oligomeric surfactants as novel air entraining agents for concrete, *Colloids and Surfaces A: Physiochemical and Engineering Aspects* **538**, 683-693 (2018).